ICESat over Arctic sea ice: Interpretation of altimetric and reflectivity profiles

R. Kwok,[1] G. F. Cunningham,[1] H. J. Zwally,[2] and D. Yi[3]

Received 18 July 2005; revised 27 December 2005; accepted 16 February 2006; published 3 June 2006.

[1] We provide an assessment of the ICESat altimeter for studying the Arctic Ocean and examine the magnitude of the large- and small-scale expressions of geophysical processes embedded in the elevation profiles. This analysis includes data from six surveys. At the large scale the response of the ice-covered ocean to atmospheric loading is near ideal (i.e., approximately −1 cm/hPa). After removal of the inverted barometer effects and best available geoid the elevation signal is still dominated by unresolved geoid residuals (∼0.4 m) that can be seen in the similarity of the remaining spatial patterns. Seasonal differences in elevations over multiyear ice are consistent with snow depth climatology; the broad differential spatial patterns are indicative of interannual differences in multiyear ice coverage associated with advection. Patterns in the derived surface roughness fields correspond to the seasonal and perennial ice zones seen in QuikSCAT data. At the small scale, near-coincident RADARSAT imagery provides a spatial context for understanding the signature of the observed elevations, waveforms, and reflectivity, in particular, those associated with thin ice, open water, multiyear ice, and ridges. The precision of the elevation estimates measured over relatively flat sea ice, identified in synthetic aperture radar (SAR) imagery, is ∼2 cm. The unambiguous identification of ridged areas in coupled ICESat/RADARSAT analysis could be used to enhance the utility of SAR imagery for examining ridge distributions. Over a 20 day period we monitored the evolution of the reflectivity of a newly opened lead. The steep increase in reflectivity due to snow coverage suggests that dips in ICESat reflectivity are likely areas of thin ice and could serve as a basis for selection of tie points for use as sea level reference. Identification of these tie points is crucial for accurate estimation of sea ice freeboard.

Citation: Kwok, R., G. F. Cunningham, H. J. Zwally, and D. Yi (2006), ICESat over Arctic sea ice: Interpretation of altimetric and reflectivity profiles, *J. Geophys. Res.*, *111*, C06006, doi:10.1029/2005JC003175.

1. Introduction

[2] ICESat was launched in January 2003. This is the first laser altimetry mission to provide large-scale mapping of the Arctic Ocean. The primary objective of the ICESat mission is to measure changes in the elevation of the Greenland and Antarctic ice sheets [*Zwally et al.*, 2002]. One secondary objective is to provide estimates of sea ice thickness, a key parameter of interest to the sea ice and climate communities. As laser altimeter observations of the sea ice cover are relatively new, the geophysical utility and limitations of these sea ice observations remain topics of investigation. A brief examination of the uses of the ICESat data set for sea ice investigations can be found in *Kwok et al.* [2004]. The present note expands on this work and focuses on the amplitude of the large- and small-scale geophysical signal embedded in the altimetric profiles. Even though we do not address directly the topic of sea ice thickness retrieval in this note, the analysis here contributes to an understanding of the natural variability in ICESat elevations and the uncertainties that limit the achievable accuracy in the estimation of sea ice freeboard and thickness.

[3] ICESat carries the Geoscience Laser Altimeter System (GLAS). This instrument consists of two channels, at 1064 nm and 532 nm, the longer wavelength of which is used for surface altimetry. With a beam width of ∼110 μrad and a pulse rate of 40/s, it samples the Earth's surface from an orbit with inclination of 94° with footprints of ∼70 m in diameter spaced at ∼170 m intervals. The Arctic Ocean is covered to 86°N. Expected accuracy in elevation determination over relatively low-slope surfaces (e.g., ice sheet) is ∼14 cm. ICESat data products provide the surface elevation, relative to an ellipsoid, derived from the altimetric waveforms. On a broad scale, the highly reflective air/snow interface dominates the echo energy from the sea ice cover. However, at a spot size of 70 m, smaller-scale features also modulate the amplitude and character of the waveforms. Ice thickness, snow depth and surface height distributions due to ridges, hummocks, and ice rafts all contribute to the variability of the reflected energy and the

[1]Jet Propulsion Laboratory, California Institute of Technology, Pasadena, California, USA.
[2]Cryospheric Sciences Branch, Goddard Space Flight Center, Greenbelt, Maryland, USA.
[3]SGT, Inc., Goddard Space Flight Center, Greenbelt, Maryland, USA.

Copyright 2006 by the American Geophysical Union.
0148-0227/06/2005JC003175$09.00

broadening of the echo waveforms. Detailed surface information is contained in the data although the interpretation requires supporting observations at close to the same spatial resolution. Near coincident synthetic aperture radar (SAR) imagery, with comparable resolution, provides a spatial context for examining these signatures and their use. With RADARSAT observations, *Kwok et al.* [2004] demonstrated an approach for unambiguous identification of thin ice and open water segments in ICESat elevation profiles. These segments of open water or thin ice (less than several centimeters thick) are crucial for locating the sea surface; a prerequisite for estimating the local sea ice freeboard in ICESat elevation as current knowledge of the time-varying sea surface height is far from adequate for direct freeboard retrieval without the introduction of tie points. Supporting high-resolution imagery is critical for interpreting small-scale variability in the elevation profiles. In this paper, we use coincident SAR data to study the elevation and reflectivity signatures of thin ice and open water in new openings, ridges, and undeformed ice. The steep increase in reflectivity of lead ice, due to rapid snow coverage in its natural environment, suggests an algorithmic basis for identification of such segments in ICESat elevation without the use of SAR imagery.

[4] Other contributions to elevation variability observed by ICESat include geoid undulations, sea surface response to atmospheric pressure loading, tides, and dynamic topography of the ocean. ICESat data products provide estimates of geoid and modeled tide elevations. Residuals after the removal of these terms are large, especially at the length scale of the ICESat footprint. The magnitude of these residuals are examined; if separable from each other they can be used to improve models of tides, geoid, dynamic topography, and the response of the Arctic Ocean to atmospheric forcing. Our current knowledge of these terms and their expected variability are discussed.

[5] This work represents a first-order assessment of the characteristics and utility of ICESat data for studying the Arctic Ocean. It examines the magnitude of the large- and small-scale expressions of geophysical processes embedded in the ICESat data. The retrieval of freeboard and thickness estimation is not within the scope of this paper. The paper is organized as follows. Section 2 describes the data sets used in this paper. Specific ICESat parameters used in our analyses and relevant ICESat instrument and data characteristics are described in section 3. The component terms that contribute to the variability in ICESat elevations are discussed in section 4. Section 5 discusses the large-scale patterns in seasonal and interannual differences in ICESat elevations. Small-scale features that are observed using near coincident ICESat/RADARSAT are examined in section 6. The last section summarizes the paper.

2. Data Description

2.1. ICESat

[6] The ICESat sea ice data set used here is acquired during six periods (three winters, two falls, and one spring); the duration and dates of these periods are shown in Table 1. Limitations of the laser lifetime have led to a revised measurement strategy from the originally intended continuous operation in a 183 day repeat orbit to a set of discrete campaigns in which the 33 day near-repeat subcycle of a 91 day orbit is surveyed at three to six month intervals. This approach was employed to allow for detection of seasonal and interannual changes in the face of an unknown mission lifetime. Heretofore, the six surveys will be refereed to as: FM03, ON03, FM04, MJ04, ON04, and FM05. The latest product releases available, at the time of this writing, are used in this paper.

Table 1. ICESat Data Acquisition Periods

Laser	Survey	Period	Repeat
1a	FM03	20 Feb–29 Mar 2003	8 day
2a	ON03	4 Oct–19 Nov 2003	91 day/33 day subcycle
2b	FM04	17 Feb–21 Mar 2004	91 day/33 day subcycle
2c	MJ04	18 May–21 Jun 2004	91 day/33 day subcycle
3a	ON04	3 Oct–8 Nov 2004	91 day/33 day subcycle
3b	FM05	17 Feb–22 Mar 2005	91 day/33 day subcycle

2.2. Other Data Sets

[7] The RADARSAT imagery used here are calibrated, processed, and archived at the Alaska Satellite Facility (ASF) in Fairbanks. The RADARSAT C-band synthetic aperture radar (SAR) transmits and receives horizontally polarized radiation (HH). All image data used here (resolution ~150 m) are acquired by the instrument operating in a ScanSAR mode, which illuminates a 460 km ground swath. The incidence angle across the swath ranges from 20° to 44°. The data from the ASF SAR processor have an absolute calibration accuracy of ±2 dB with a relative calibration accuracy of ~1 dB. Since November 1996, there is near 3 day RADARSAT coverage of the Arctic Ocean acquired as part of a NASA program to study the small-scale kinematics of sea ice. To support ICESat studies, the frequency of coverage was increased for the FM04, MJ04, ON04, and FM05 surveys. Gridded multiyear ice fractions are from analysis of QuikSCAT data [*Kwok*, 2004]. QuikSCAT is a moderate resolution wide-swath (1800 km) K_u-band scatterometer that provides daily coverage of the Arctic Ocean at V- and H-polarizations at incidence angles of 53° and 45°. Six-hourly sea level pressure (SLP) fields are from the National Centers for Environmental Prediction (NCEP)–National Center for Atmospheric Research (NCAR) reanalysis products [*Kalnay et al.*, 1996]. The uncertainties in the NCEP sea level pressure analyses are not well known. One comparison with ship measurements [*Smith et al.*, 2001] reports differences of less than 2 hPa in the tropics and midlatitudes to over 4 hPa in the polar regions.

3. ICESat Data Characteristics

[8] A brief description of the relevant instrument and data characteristics necessary for the interpretation of the altimeter profiles is provided in this section. The GLAS instrument records the time-dependent surface returns (waveforms) from each laser shot or pulse. The laser footprint on the surface is nominally 70 m. The width of the transmitted pulse is 4 ns, equivalent to ~60 cm in surface elevation. The shape of the echo waveform is affected primarily by the transmitted pulse shape, the surface height distribution within the footprint, and forward scattering in the atmosphere. The return waveforms are sampled every nanosecond (15 cm). Over sea ice, an

on-board algorithm selects 200 samples around each detected pulse for transmission to the ground. In the absence of forward scattering by clouds, the typical sea ice waveform resembles a single-peak Gaussian. Forward or multiple scattering from cirrus clouds affects the trailing edge of the waveform, so that it is no longer Gaussian. The peak location of a Gaussian fitted to the waveform is used to determine the centroid of the surface return and its range. From ground tests, *Yi et al.* [2003] estimate an uncertainty of ~2 cm due to this fitting procedure; additional sources of uncertainties are those that affect pulse shape described above. Detailed descriptions of the procedures used in the estimation of the absolute elevations can be found in *Brenner et al.* [2000]. *Zwally et al.* [2002] estimate that the elevation uncertainty of a single laser shot to be ~14 cm; this includes uncertainties in orbit determination (5 cm), attitude determination (7.5 cm), atmospheric delay (2 cm), atmospheric forward scattering (2 cm), and unmodeled errors (1 cm). The analyses presented in this paper use three instrument and waveform-derived parameters from the ICESat data products: i_reflctUcorr (R), i_gainSet1064 (G), and i_SeaIceVar (S). R is the reflectivity (not corrected for atmospheric effects) and is the ratio of the received energy after it has been scaled for range, and transmitted energy; the reflectivity is not a calibrated quantity because of uncompensated detector saturation issues (discussed below) and atmospheric attenuation. G is the time-varying gain setting of the detector; and S is the difference between the fitted Gaussian and the received waveform. These parameters provide qualitative measures of the reliability of the retrieved elevation. A high G indicates that the signal-to-noise ratio (SNR) is low and thus the likelihood of reduced surface return because of scattering by atmospheric constituents (clouds, water vapor etc). In this work, all samples with $G > 50$ are removed; detector gain varies between 7 and 250. This is an empirically determined threshold intended to remove unreliable low SNR samples that are contaminated by atmospheric scattering associated with clouds and water vapor. S is a measure of the deviation of the waveform from an expected Gaussian-like return; $S = 0$ for a perfect Gaussian. Large Ss indicate larger deviations and the uncertainty of the retrieved elevation from any non-Gaussian waveform is likely higher.

[9] Because of the limited dynamic range of the instrument, a fraction of the waveforms are saturated. Saturation can be caused by (1) the natural reflectivity of the surface and (2) the time-varying transmitted laser pulse energy associated with the age and particular characteristic of the three lasers on GLAS. The severity of waveform saturation depends on received echo energy. Higher pulse energy provides higher SNR but also increases the likelihood of detector saturation. Conversely, reduced pulse energy lowers SNR. When saturation occurs, the estimated elevation becomes less reliable as the peaks of the waveforms become distorted making the waveform less Gaussian-like; the additional uncertainty is dependent on the level of saturation. For moderate saturation of the GLAS detectors, the shape of the return pulse leading edge up to the onset of saturation is properly recorded, but the width of the pulse, the characteristic abrupt decrease in amplitude at the trailing edge, and subsequent detector "ringing" (amplitude oscillations about the background level) are artifacts. These effects introduce additional delays or biases in the range estimation process [*Brenner et al.*, 2000].

[10] These delays can be modeled: there is an empirical relationship between E_r (after onset of saturation) and the added time delay (Δt) even though the waveform is distorted and E_r is not accurately measured. On the basis of ground equipment tests, a deterministic correction to the estimated elevation has been developed to account for this saturation effect [*Sun et al.*, 2003]; the time delay is adjusted based on the received echo energy, E_r (in femtojoules (fJ)):

$$\Delta t(ns) = \begin{cases} 0 & \text{for} \quad E_r < 9fJ \\ 0.68706 - 0.30919E_r + 4.9006 \times 10^{-2}E_r^2 - 3.2897 \times 10^{-3}E_r^3 + 8.5389 \times 10^{-5}E_r^4 & \text{for} \quad 9fJ \le E_r < 16fJ. \\ -1.9426 + 0.14868E_r & \text{for} \quad 16fJ \le E_r \end{cases}$$

The coefficients used here are results from the most recent test data set. The onset of saturation is at 9 fJ. The uncertainties in the corrections are 2 cm for E_r below 40 fJ and 7 cm for E_r between 40 fJ and 140 fJ (X. Sun, personal communication, 2005).

[11] The effect of saturation can be seen in the distributions of E_r and S for the six Arctic Ocean surveys shown in Figure 1. As expected, E_r is directly related to the transmitted pulse energy (not shown here). The correlation between E_r and S highlights the saturation issue. Typically, one does not expect S as defined to be significantly correlated to E_r because the shape and amplitude of the waveform should be dependent only on surface characteristics and relatively independent of E_r. Although unlikely, some sea ice features could have high reflectivity as well as non-Gaussian returns. In this case, the observed correlation is most likely due to saturation. For the ON04 survey, E_r explains more than 74% of the variability in S. The mean E_r, except for the FM04 and MJ04 surveys, are all above 9 fJ (but below 20 fJ) and thus a large fraction of the waveforms are affected by saturation. At 16 fJ, the correction at ~7 cm is moderate. The MJ04 survey, with the lowest mean E_r, also exhibits low correlation; the large variability of S in this case is likely due to lower SNR. As seen later, this survey provided the smallest number of valid data samples after our data filters described above. Also likely is the reduced echo from the surface due to increased water vapor in the atmosphere during the onset of spring melt in the Arctic Ocean. From a saturation perspective, the FM04 data set seems to have the highest quality with mean $E_r \sim 10$ fJ and low ρ^2; the variability of these two parameters are also the lowest. The effectiveness of the

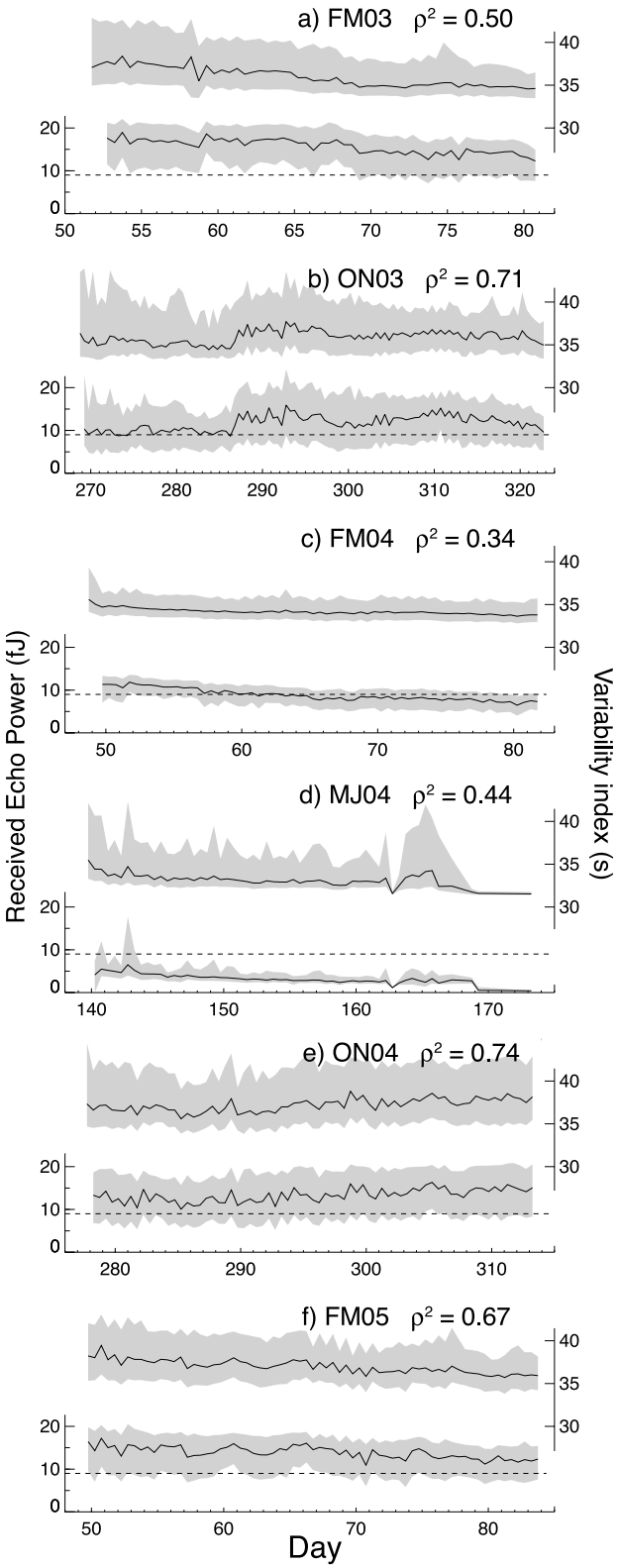

Figure 1. Distribution of received echo power (in femtojoules) and sea ice variability index (s) from the six surveys. (a) FM03. (b) ON03. (c) FM04. (d) MJ04. (e) ON04. (f) FM05. Variable s is a measure of the deviation of the altimeter waveform from a fitted Gaussian. Variable ρ^2 is the squared correlation between the two detrended time series. The variability of these parameters is shown in gray. The onset of saturation starts above the dashed line (at 9 fJ).

saturation correction to near-specular targets, with severely distorted waveforms, is illustrated in section 6.

4. Variability of ICESat Elevations

[12] The retrieved surface elevation, h_{obs}, can be written as

$$h_{\mathrm{obs}}(x,t_i) = h_f(x,t_i) + h_{\mathrm{ssh}}(x,t_i) + \varepsilon(x,t_i), \quad (1)$$

where h_f is the sea ice freeboard and h_{ssh} is the sea surface height relative to a particular reference ellipsoid (TOPEX/Poseidon in the case of ICESat); ε is the instrument noise ($\sim$14 cm as discussed above) and uncertainties in the range estimation process. Variable h_{ssh} can be further decomposed into the following terms:

$$h_{\mathrm{ssh}}(x,t_i) = h_g(x) + h_a(x,t_i) + h_T(x,t_i) + h_d(x,t_i) + O^2, \quad (2)$$

where h_g is due to geoid undulations, h_a represents the sea surface response to atmospheric pressure loading, h_T is from tidal contributions, h_d is the dynamic topography associated with geostrophic surface currents, and second-order terms. Here, sea ice freeboard, h_f, is defined as the distance between the local sea surface and air-snow interface, and is the sum of the snow and ice components. Except for h_g (which we assume to be constant over the timescales of interest), the remaining terms are time varying. Knowing h_{ssh} is of obvious importance for accurate derivation of freeboard although our current knowledge of the sea surface is far from adequate for direct freeboard retrieval without the introduction of tie points; centimeter level knowledge is required. Thus an understanding of the spatial and temporal length scales and variability of each of the contributing terms in the equation helps not only in the interpretation of the altimetric profiles but also in the determination of the number of tie points required for optimal estimation of the sea surface as well as the uncertainties associated with the estimation process. Below, we describe briefly the expected variability of each term in equation (2).

4.1. Variability Due to h_a

[13] The 8 day exact repeat orbits from the FM03 survey are ideal for examining the variability in h_{obs} associated with atmospheric loading and the geoid. Subsequent surveys are less ideal because of the lack of short period near exact repeat orbits. Figure 2 shows six repeat pass elevation profiles (after the along-track samples are aligned) of two orbits from the three 8 day cycles in FM03. The elevation profiles are clearly dominated by residuals in h_g (after removal of the ArcGP geoid, discussed below) that range up to 2 m. Assuming the changes in the 25 km median values in h_f to be small during the 8 day period, the remaining variability should be entirely due to h_a, h_d, uncertainties in the tide model and measurement noise (ε). Figure 3b shows a map of the elevation differences between two eight day repeat cycles; the sample population of $\sim$1.9 million has a mean difference of 10 cm and standard deviation of 25 cm. This is a large reduction in variance of the field (compared to meters) as h_g, the common term, is temporally invariant and consequently removed in the differencing process.

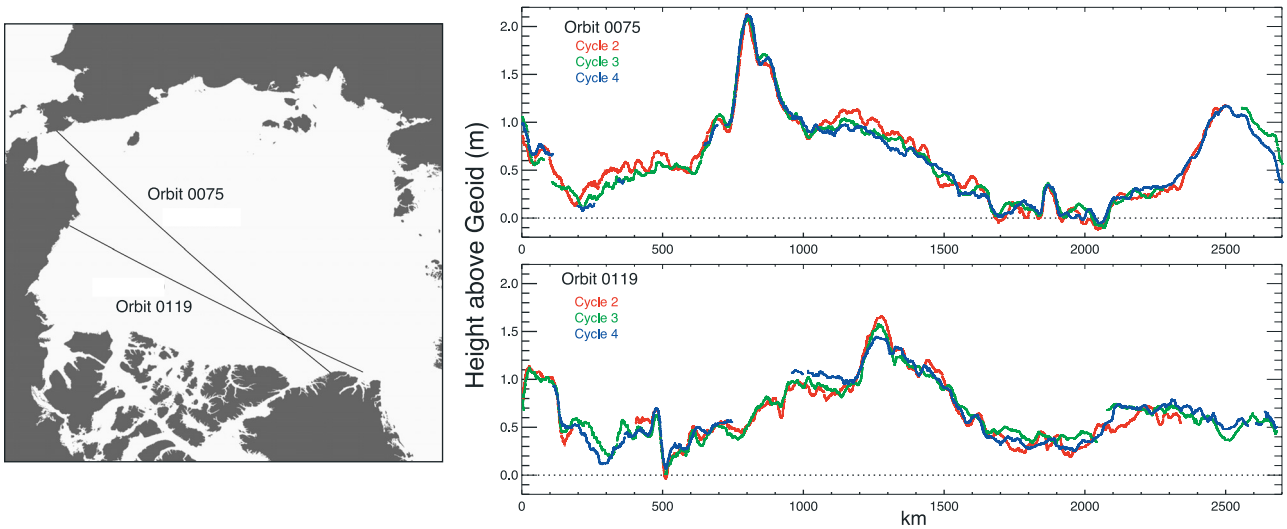

Figure 2. Sample elevation profiles from two exact repeat ground tracks (8 day separation) from FM03 after removal of the updated ArcGP geoid and tidal effects. Samples are 25 km median elevations.

[14] The response of the sea/ice surface to atmospheric loading can be seen in the regression of the differences in ICESat elevations (Δh) upon differences in sea level pressure (ΔP) of all the data samples between two 8 day exact repeat cycles from FM03 (Figure 3a). Sea level pressure at each ICESat sample is linearly interpolated from 6-hourly NCEP-NCAR reanalysis products. Over this period, it can be seen that ΔP has a range of more than 70 hPa, or equivalently 70 cm in sea level. The regression coefficient is -1.12 cm/hPa with a correlation of -0.81 between the two variables. This magnitude is somewhat higher than the ideal inverted barometer effect (IBE: the isostatic response of sea surface height to changes in atmospheric pressure) of -1 cm/hPa. This departure from ideal IB response can be attributed to a number of factors: the dynamic response of sea level to wind stress that is correlated to pressure in its own way, the nonstatic behavior of the ocean, the residuals in the observed elevation, and errors in the atmospheric pressure data set. In fact, *Pihos* [1994] used a long time series (>1 year) of TOPEX/POSEIDON altimeter data of the oceans south of 66°N to show that the response of the sea surface height is close to ideal IB when the wind-forced component of the observed elevation is removed. Thus the atmospheric response, h_a, should be further separated into one component that is dependent on the isostatic response h_{IB} and another that is dependent on wind stress h_{ws}. Compared to the lower-latitude oceans, the effect of the wind-forced component on sea level is not as well understood because of the sea ice cover. The lengths of our data sets, however, are too short to allow for a similar study to decouple these effects over the Arctic Ocean. Similarly, nonideal IB behavior is expected over shallow waters and is a subject of research [*Wunsch and Stammer*, 1997]. For altimetric purposes, it is evident that the IB correction significantly decreases the variance of sea level and is an important step in using the data. As pointed out by *Wunsch and Stammer* [1997], what is much less obvious is the extent to which the residuals represent a dynamic response of the ocean to pressure loading.

[15] The effect of applying the IB correction can be seen in the reduction in variance in the elevation differences between two 8 day repeat cycles (Figures 3b and 3c). The resultant mean of 1.5 cm and standard deviation of 15 cm represent a tenfold reduction in mean and a twofold reduction in variability. Overall, the near zero mean seems to indicate that there is relatively little bias in the ICESat elevations over the two 8 day periods. Except for samples in the Canadian Archipelago and the coastal regions of the Laptev and Kara Seas, the difference field in Figure 3c seems spatially uniform. Potentially, the variability due to tides and dynamic topography may dominate in the narrow passages in the Canadian Archipelago and on the broad shelves of the E. Siberian Sea.

4.2. Variability Due to h_g

[16] The spatial variability of h_g is more energetic than h_T, h_a, and h_d at all length scales [*Chelton et al.*, 2001; *Wagner*, 1979]. The best available geoid of the Arctic region is that produced by the Arctic Gravity Project (ArcGP) [*Kenyon and Forsberg*, 2001] and has a grid spacing of $5' \times 10'$ (latitude $\times$ longitude). The spatial details in the ArcGP geoid can be seen in the shaded relief map in Figure 4c. The elevation field after the IB, tides, and ArcGP geoid corrections is shown in Figure 4a. The residuals (Mean: 0.37 m; S.D.: 0.55 m) due to unmodeled geoid features can be clearly seen. The same plot except with an updated ArcGP geoid [*Forsberg and Skourup*, 2005] is shown in Figure 4b. A significant reduction in the variance of the elevation field is evident. By incorporating GRACE (Gravity Recovery and Climate Experiment) observations, a large fraction of the longer length scale geoid features are now correctly modeled thus reducing the residuals in the h_{obs}-h_g-h_T-h_{IB} field (Mean: 0.04 m; S.D.: 0.38 m). The GRACE estimates have a geoid height accuracy of 2–3 mm at spatial resolutions as small as 400 km [*Tapley et al.*, 2004]. Figure 5 shows the residual elevations in the six surveys after the removal of this updated geoid. It is apparent from the similarity in the spatial patterns of the elevation fields that the largest signal is in the unresolved spatial details of the

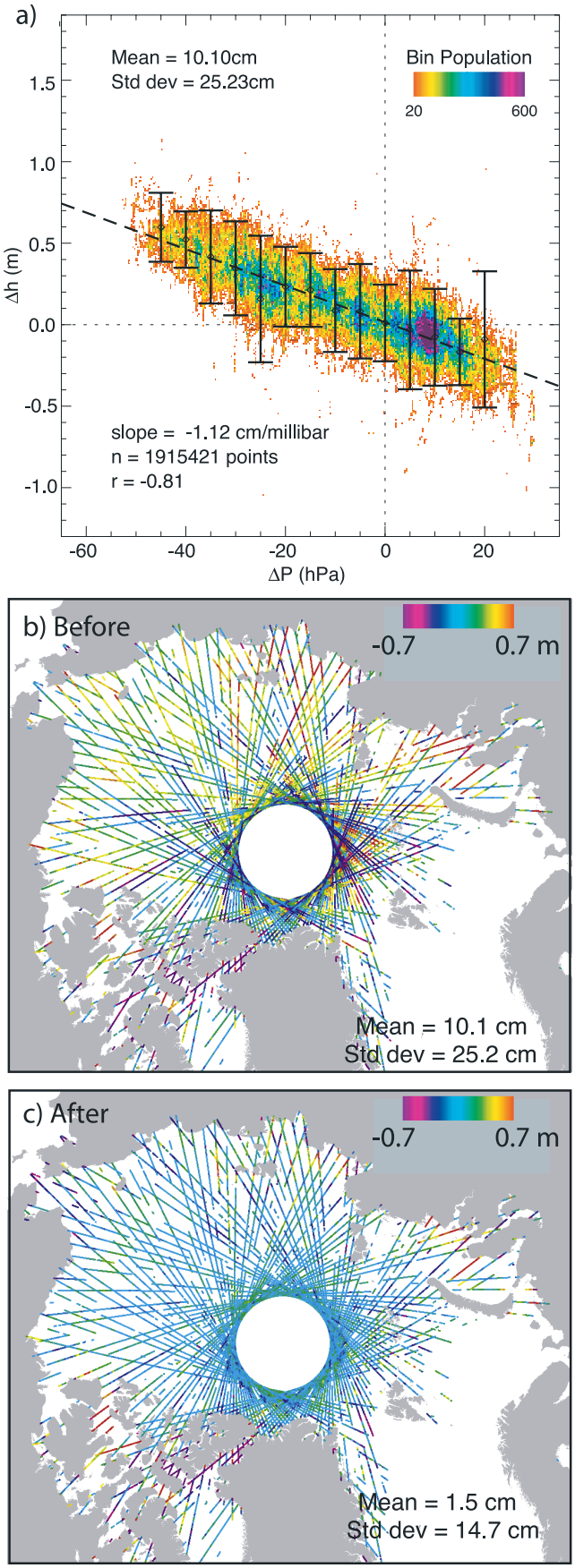

Figure 3. Response of ICESat elevations to sea level pressure. (a) Regression of elevation differences (Δh) against differences in sea level pressure (ΔP). Differences are between two 8 day exact repeat cycles during the FM03 survey. Maps show the elevation variability (b) before and (c) after removal of inverted barometer effect. Sea level pressures are from the 6-hourly NCEP-NCAR reanalysis products.

geoid that are not represented in the GRACE-ArcGP geoid. Features in the residual field correspond to bathymetric relief with high surface slopes. For example, the shelf break north of the E. Siberian Sea and the Nansen Ridge are rather prominent. It is also evident that these residuals, from ICESat, could be used to improve the smaller-scale features in the Arctic geoid.

4.3. Variability Due to h_T

[17] Model elevations of h_T due to ocean, load, and solid earth tides are provided in the ICESat products. Elevations of ocean tides are from the GOT99.2 tide model (GOT = Goddard/Grenoble Ocean Tide) [*Ray*, 1999]. The solutions are primarily based on the tidal analyses of 6 years of TOPEX/Poseidon altimeter data supplemented with several hydrodynamic models in shallow and polar seas. Global tide models developed with the use of TOPEX/Poseidon altimetry have accuracies in the range of 2–3 cm [*Shum et al.*, 1997]. However, this assessment is only good where TOPEX observations are available, i.e., south of 60°N. The tidal solutions from regional Arctic Ocean models are poorer. An intercomparison of three tidal models of the Arctic Ocean reported by *Peacock and Laxon* [2004] indicates that the main tidal constituents predicted by these models agree to only within ~6–8 cm. The models are: the FES95.2.1 of *Le Provost et al.* [1998], the CSR3.0 model of *Eanes* [1994], and the model of *Kowalik and Proshutinsky* [1994]. It should be noted that the ocean tides in certain areas of the Arctic (e.g., Baffin Bay) could be more challenging.

[18] The magnitude of the ocean load tide correction is typically less than 10 cm, with an accuracy of better than 1 cm [*Cudlip et al.*, 1994]. Finally, the solid Earth tide varies globally in the range ±30 cm, with an uncertainty of much less than 1 cm [*Cudlip et al.*, 1994]. The corrections in the Arctic indicate that the values are generally less than 2 cm, considerably less than the typical global values.

4.4. Variability Due to h_d

[19] Time varying dynamic topography, h_d, of the Arctic Ocean is not well known and not provided as part of the ICESat data products. On the basis of two years of satellite altimetry, *Peacock and Laxon* [2004] investigated the variability in sea surface height (on a 0.25° × 0.25° grid) after the removal of tidal and atmospheric contributions. They report an RMS value for the crossover differences of mean sea surface profiles of 4.2 cm in the ice-covered Canada Basin, compared with 3.8 cm in the ice-free Greenland-Iceland-Norwegian Seas. In that work, comparisons made with an existing global mean sea surface (OSUMSS95) highlight significant differences between the two surfaces in permanently ice-covered seas; the model perhaps under-

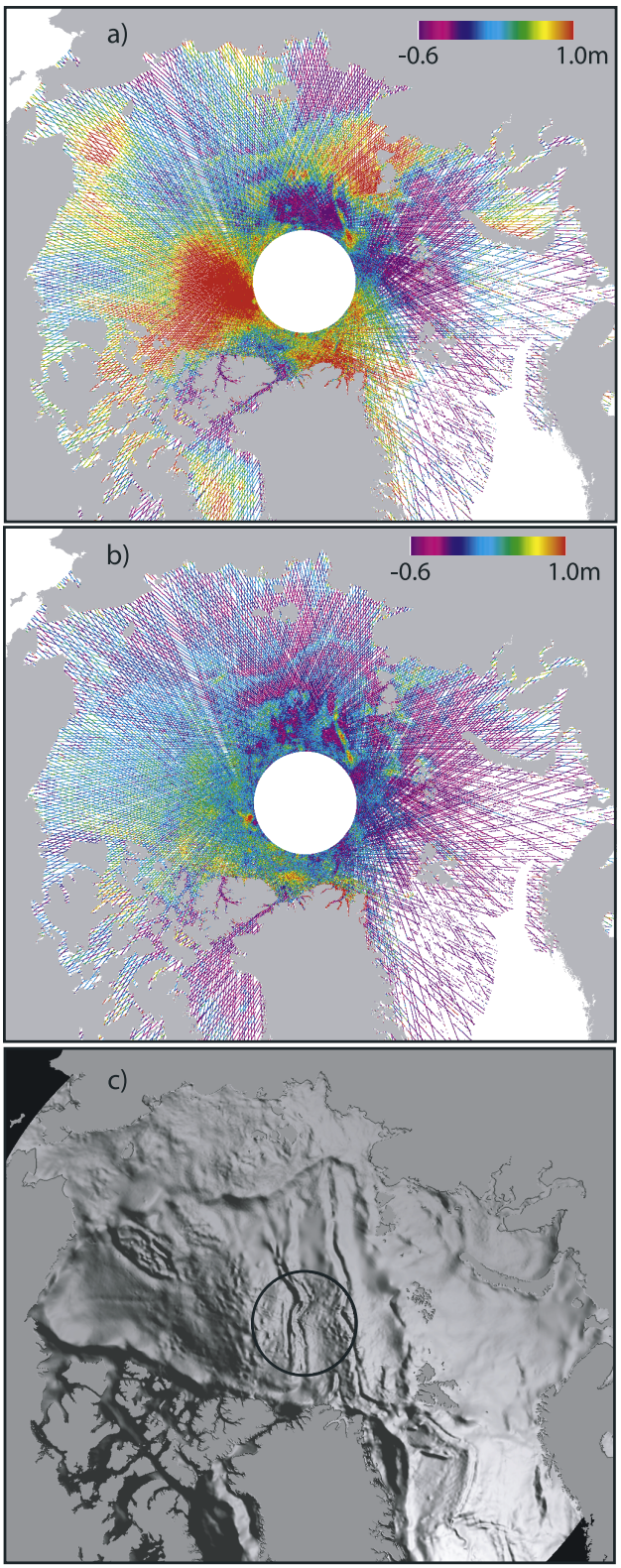

Figure 4. (a) Comparison of the ICESat elevation fields after removal of the ArcGP geoid. (b) updated ArcGP geoid [*Forsberg and Skourup*, 2005]. Tidal and inverted barometer effects (discussed in the text) have been removed. (c) A shaded surface representation of the ArcGP geoid. These composites are constructed using data from the FM04 survey and represent 480 orbits with more than 5.5×10^6 elevation samples.

estimates the variability. In addition, they indicate that both model and altimetry show some correlation with bottom topography. The model simulations reveal a strong topographic control, characteristic of barotropic flow in the Eurasian and Canada Basins and in the Arctic marginal seas, where relatively strong transports are confined mainly to the continental shelves.

[20] Figure 6 shows the standard deviation of sea surface height for 2003 from a particular integration of the cubed sphere eddy-permitting global model configuration (on an 18 km grid), which is forced by NCEP reanalysis winds and atmospheric conditions, excluding tides and atmospheric pressure forcing. This simulation is produced by the Massachusetts Institute of Technology general circulation model (MITgcm [*Marshall et al.*, 1997]) with the global ocean and sea ice configuration of *Menemenlis et al.* [2005]. In response to atmospheric forcing and to internal variability, the model predicts fluctuations ranging from 2.5 cm in the central Arctic up to 25 cm in shallow coastal regions. While these models do not resolve eddies they do provide a lower bound on the expected contributions from dynamic topography. Significant variability can be expected from this term especially over the shallow shelves of the Arctic Ocean.

5. Large-Scale Variability

5.1. Seasonal and Interannual Variability

[21] Here, we examine the seasonal and interannual differences in the elevation fields shown in Figure 5. Again, in the differencing process, the common term h_g is removed. Assuming that h_T and h_a are modeled correctly, the residual variability are due to h_d and h_f. In seasonal differences, between the February/March surveys and the October/November surveys (winter minus fall), we expect a positive mean difference in the ICESat elevations because of ice growth and the development of a snow cover after freeze up. The data from MJ04 are not used here because of the limited coverage. As a rough estimate, the contribution of the ice growth to h_f over multiyear (MY) ice would be ~5 cm (or 0.5 m of growth between October and February [*Untersteiner*, 1961]); the increase in freeboard would be higher if ridging were included. The contribution of snow depth would be ~12 cm [*Warren et al.*, 1999, Figure 13]. This value of snow depth is the difference in the mean snow depth of all the "North Pole" drifting stations, operated by the Soviet Union, between October and February (1954–1991). Over first-year (FY) ice, the contribution from ice growth would be higher and the snow depth would perhaps be lower. However, there is no climatology of snow depth over first-year ice to speak of. In any case, these provide rough constraints on the magnitude of the numbers we expect to see. Another broad constraint is that the winter-to-winter variability in the MY freeboard should typically be smaller or comparable to the snow depth, and at least smaller than the winter and fall differences.

[22] One complicating factor in assessing the elevation differences is the varying spatial coverage of MY ice from year-to-year due to advection. A simple spatial difference between the elevation fields would mix differences from FY and MY samples; this is illustrated in Figure 7. Figures 7a and 7b show the fractional MY coverage in February 2004 and February 2005 derived from QuikSCAT data [*Kwok*,

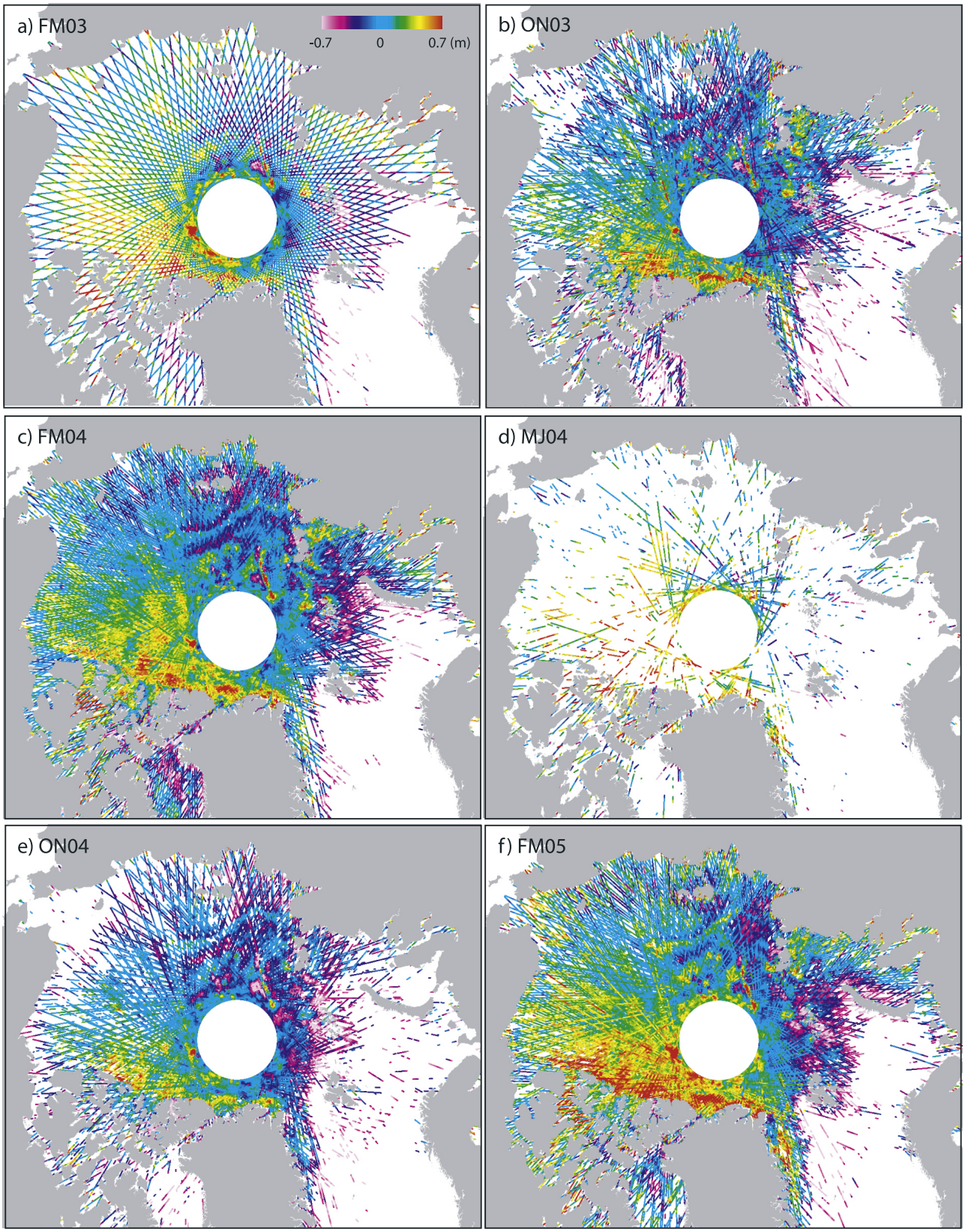

Figure 5. ICESat elevations after removal of updated ArcGP geoid and tidal and inverted barometer effects for all six surveys. (a) FM03. (b) ON03. (c) FM04. (d) MJ04. (e) ON04. (f) FM05. Map samples are median elevations on a 10 km grid.

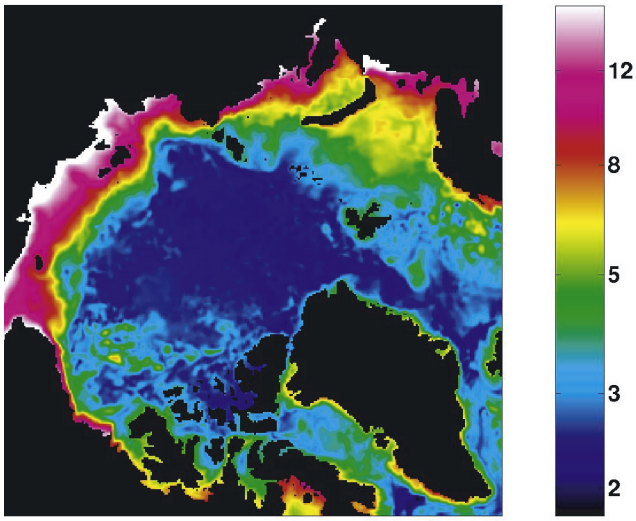

Figure 6. Standard deviation of sea surface height for simulation year 2003 from a particular integration of model described in text, excluding tides and atmospheric pressure forcing. Units are centimeters. The simulated variability ranges from 2.5 cm in the central Arctic to 25 cm in shallow coastal regions (provided by D. Menemenlis).

2004]. The spatial difference (Figure 7c) shows large differences in MY fraction over the Nansen Basin because the edge of the perennial ice zone is located farther north in February 2005. This is evident in the differences in the ICESat elevation fields between FM05 and FM04. Rather than a result of the thinning of the ice cover, the significantly lower elevation (>20 cm) over the Nansen Basin is due to an absence of MY ice in that region in FM04 (Figure 7d). This illustrates not only the importance of considering the ice types and their age when interpreting the differences between elevation fields, but also the sensitivity of the ICESat elevation to such differences. To account for advection, the time-varying h_f should be ideally evaluated within a Lagrangian parcel of ice. However, available observations do not allow such an approach.

[23] Our approach is to examine the seasonal differences shown in Figure 8 by separating the elevation estimates into two populations: one where the samples have MY fraction > 0.9 in both surveys and the other where MY fraction < 0.25. Again, the MY fractions are derived from colocated QuikSCAT data [*Kwok*, 2004]. First, the differences between the February/March surveys in both the FY and MY populations are smaller than the differences between the February/March and October/November surveys. They satisfy the seasonal constraint set forth above. Second, the magnitude of the differences between the February/March and October/November surveys are not far from that of ~12 cm [*Warren et al.*, 1999], recognizing that the elevations considered here include contributions from h_d and residuals from all the other terms. The mean differences and variability in freeboard are higher in regions with seasonal ice; probably an indication that the changes in ice growth, snow depth, ridging, and perhaps h_d are higher in the seasonal ice zone.

[24] Naturally, this assessment of the time-varying freeboard would be more accurate after we had improved estimates of the sea surface. However, this exercise serves to demonstrate the potential and the quality of the ICESat elevations even when sea surface height tie points are unavailable. The observational implications are interesting: if we had an uninterrupted time series of data from a GLAS-like instrument to monitor the weekly or monthly changes in freeboard, it may be possible to estimate the snow depth over MY ice if basal ice growth over MY can be roughly modeled.

5.2. Sea Ice Roughness

[25] The second moment of the ICESat elevation samples along a track can be used as a large-scale measure of roughness. Smaller-scale roughness associated with the broadening of the waveform within a footprint is discussed in the next section. Figure 9 shows the spatial pattern of the standard deviation of detrended ICESat elevations over a 25 km moving window. The approximate range of roughness is from several centimeters to ~30 cm. Overall, the ice cover is roughest north of Ellesmere Island and Greenland (~30 cm), less so over much of the MY ice cover of the central Arctic (~15 cm), and smoothest in the seasonal ice zone (<10 cm). Except for FM05, the transition in roughness from the seasonal ice zone to the perennial ice zone (PIZ) can be clearly seen. The boundary between the two zones (the black contour in each figure) is derived from QuikSCAT: a K_u-band scatterometer with spatial resolution of the order of 10 km [*Kwok*,

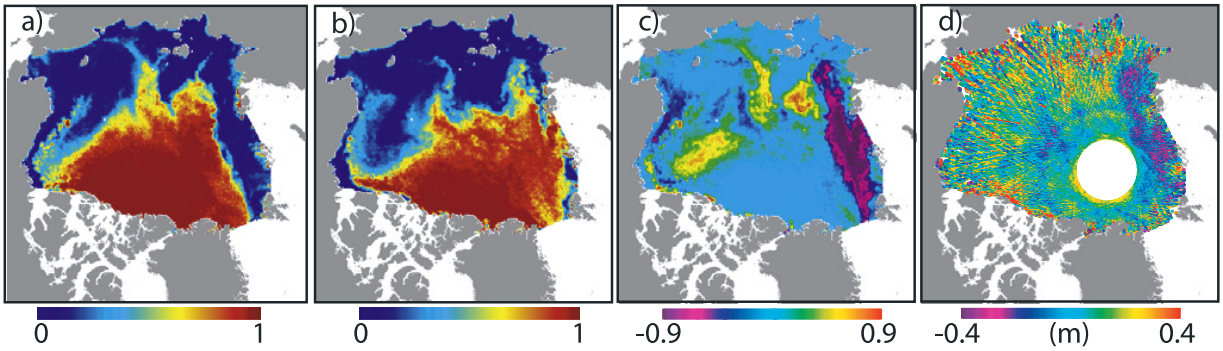

Figure 7. Comparison of spatial pattern in elevation differences between FM05 and FM04 surveys and multiyear ice coverage from QuikSCAT backscatter [*Kwok*, 2004]. (a) February 2004. (b) February 2005. (c) Differences between Figures 7a and 7b. (d) ICESat elevation differences.

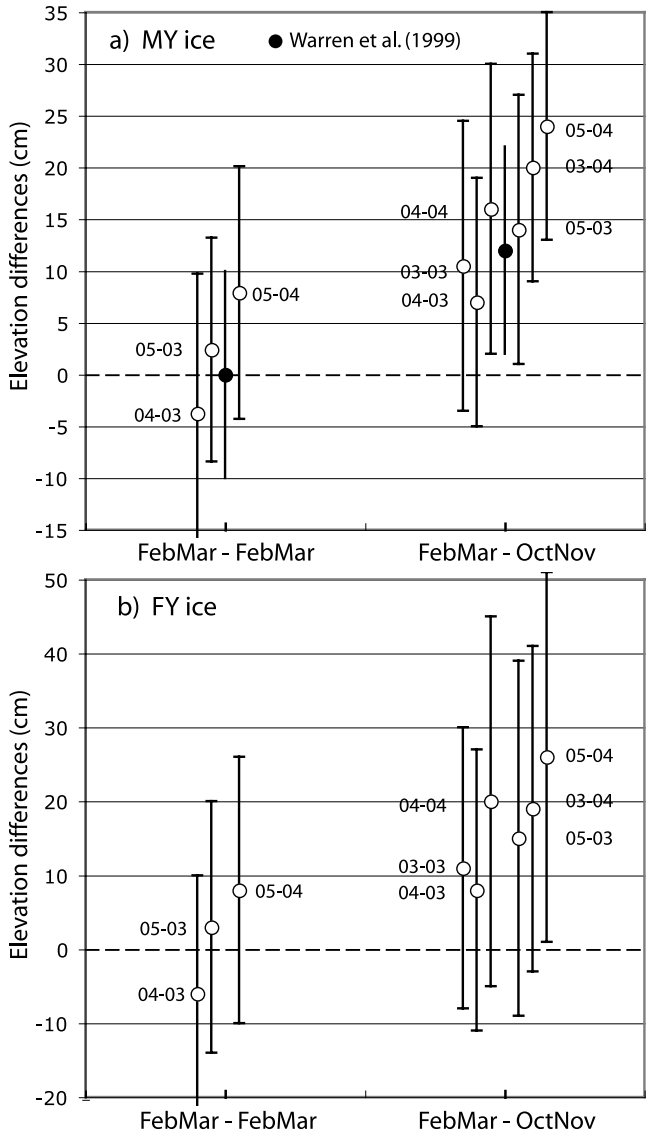

Figure 8. Seasonal differences in ICESat elevations between February/March and October/November surveys over (a) multiyear ice and (b) first-year ice. Climatological differences in mean Arctic Ocean snow depth between February/March and October/November [*Warren et al.*, 1999] are shown as solid circles.

2004]. Distinct differences in the backscatter from FY (lower backscatter) and MY (higher backscatter) ice in the scatterometer fields are used to delineate the two zones. Even though the radar scattering cross section is dependent on more than just surface roughness, the correspondence between the changes in surface roughness and backscatter in the transition from the PIZ to the SIZ is quite remarkable. The roughness pattern seems to be seasonally (i.e., during a given winter) consistent, i.e., the ON03 and FM04, and ON04 and FM05 fields are similar. The higher roughness of the FM05 survey seems anomalous; at this writing, we believe that it is associated with data artifacts rather than an actual increase in surface roughness; this requires further investigation. These surface roughness fields, in conjunction with the subfootprint roughness from waveforms, could be potentially useful for better description of the regional variability of the air/ice and ice/ocean drag coefficients used in the calculation of air/ice/ocean momentum exchanges.

6. Small-Scale Variability

[26] Near coincident RADARSAT imagery and ICESat elevations are used to examine the variability of the elevation associated with openings, ridges, older ice, and relatively flat ice. The spatial resolution of the ScanSAR imagery used here is ~150 m and is comparable to the spot size (70 m) illuminated by the beam width of the ICESat laser. The imagery provides a spatial context, along with the vertical dimension of the altimeter profiles, for better interpretation of the small-scale characteristics of the ICESat elevations.

6.1. New Openings

[27] It is evident from the discussion in section 4 that centimeter level knowledge of the time-varying sea surface height h_{ssh} compared to that required for determination of freeboard is not known. To determine freeboard in ICESat elevation profiles, one has to first identify reference samples (tie points) along the ICESat segments with known sea surface heights. *Kwok et al.* [2004] show one approach for obtaining such samples by identifying new openings using near coincident ICESat segments and RADARSAT imagery. Using the same approach, Figure 10 shows two additional examples of the ice cover before and after opening events: the thin ice areas with low radar backscatter are associated with dips in elevation and reflectivity. The time separation between the images are ~1 day and ~12 hours, respectively. The elevation/reflectivity profiles along both 80 km ICESat tracks are within ~2 hours of the RADARSAT acquisitions. Thus the age of the ice in both leads are less than a day old and in winter should have a thickness of <~10 cm or freeboard of 1–2 cm. Certainly, thin ice identified using this approach is unambiguous and would be useful as sea surface references for freeboard retrieval. However, this approach is dependent on the availability of near coincident SAR image acquisitions.

[28] Without supporting SAR imagery, we know that local minimums/dips along ICESat profiles are areas of "thinner" ice (though not necessarily thin ice) and sometimes these segments are also associated with local dips in reflectivity. Whether reflectivity is a useful criterion for unambiguous identification of thin ice is conditional on its dependence on ice thickness and snow cover. Clearly, thin ice-filled leads (e.g., frazil, nilas, gray ice, etc.) have lower reflectivity than the adjacent snow-covered ice and thick ice (Figure 11a). Figure 11b shows the observed dependence of sea ice albedo (reflectivity) to snow coverage over thin ice. After formation of a thin ice layer, the evolution of reflectivity has a stronger dependence on snow depth than thickness. It takes only ~1–2 cm of snow to mask out the reflectivity of the underlying ice; the snow covered thin ice becomes indistinguishable from the adjacent snow cover. This steep increase in reflectivity indicates the high likelihood of thin ice when dips in reflectivity and elevations are simultaneously encountered in ICESat samples. In the Arctic, anecdotal evidence indicates that open leads fill

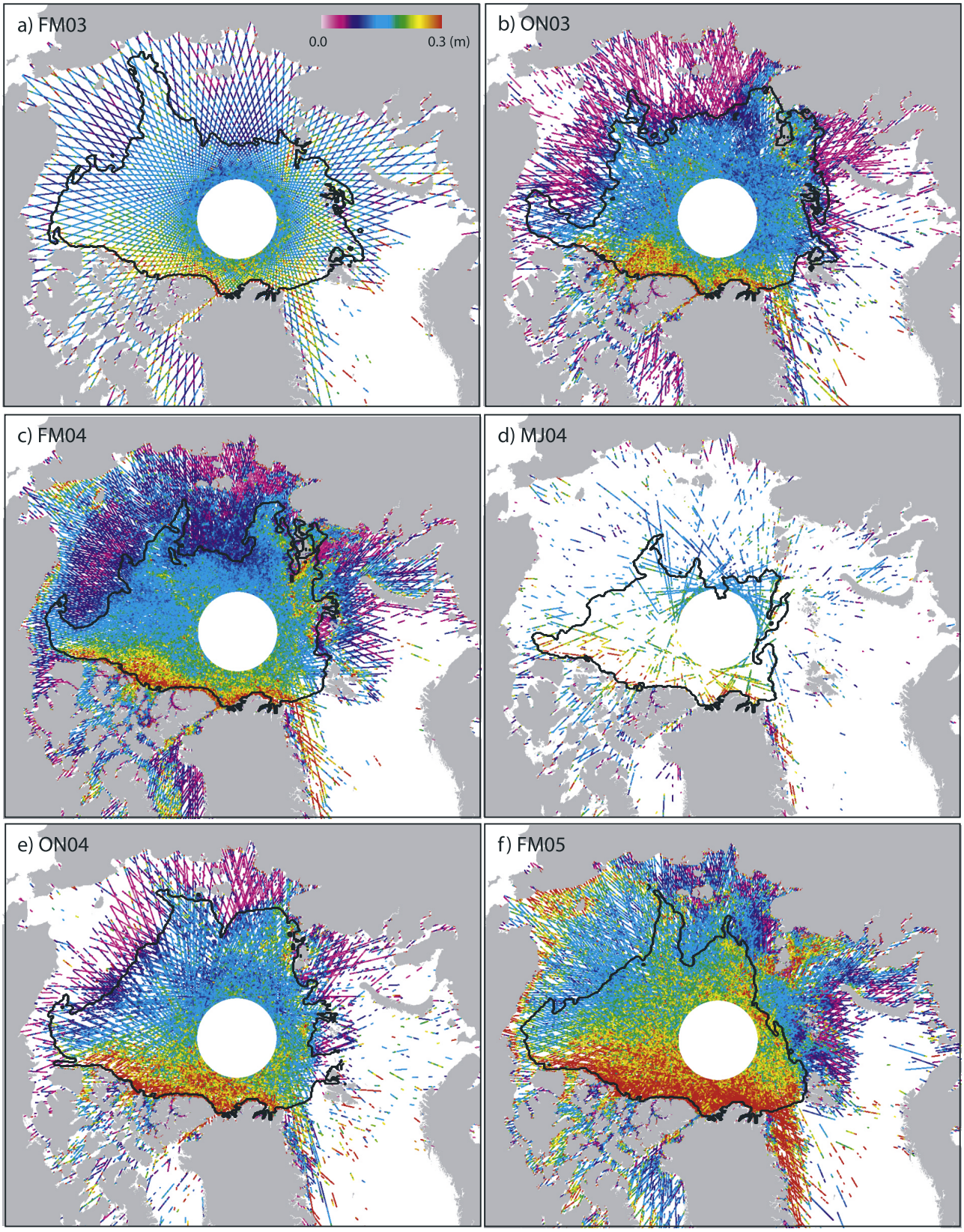

Figure 9. Surface roughness at a 25 km length scale from ICESat elevations. (a) FM03. (b) ON03. (c) FM04. (d) MJ04. (e) ON04. (f) FM05.

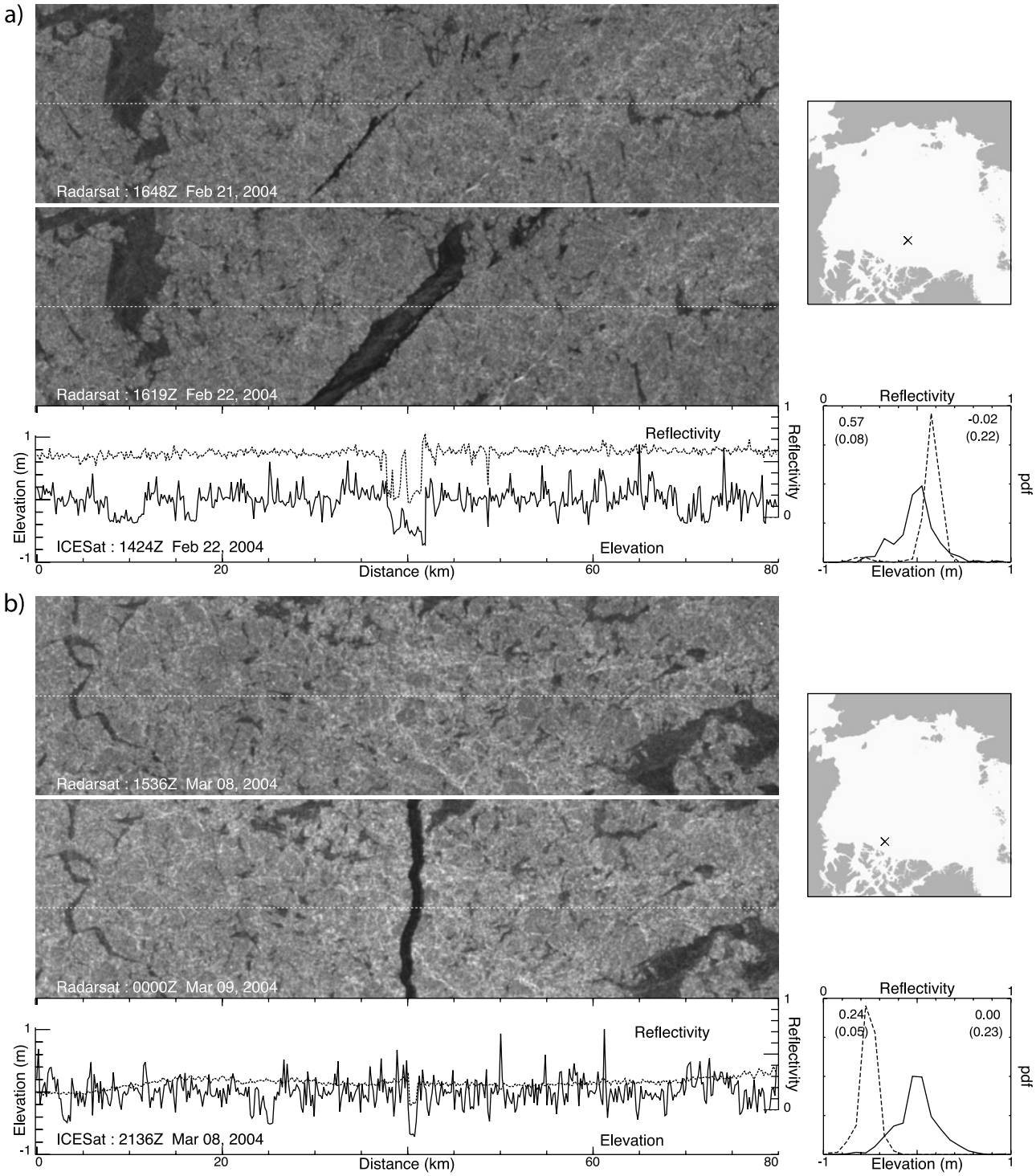

Figure 10. (a, b) Two examples of near-coincident RADARSAT and ICESat data takes over new openings. Openings in the ice cover can be seen as new areas of low backscatter after the event in time-separated RADARSAT imagery. In both examples, the ICESat track (white dashed line) and the second RADARSAT image are separated by less than 3 hours. The direction of flight is from left to right. The time separation between the ICESat and RADARSAT overflights can be computed from the date/time on the plots. The crosses on the maps mark the location of the 80 km profiles of ICESat elevations (solid) and reflectivity (dashed). Mean elevations of 25 km have been removed. Distributions of elevation and reflectivity of the samples are shown in the bottom right panel; mean and standard deviation of elevation/reflectivity are shown on the top right/left (RADARSAT imagery ©CSA 2004).

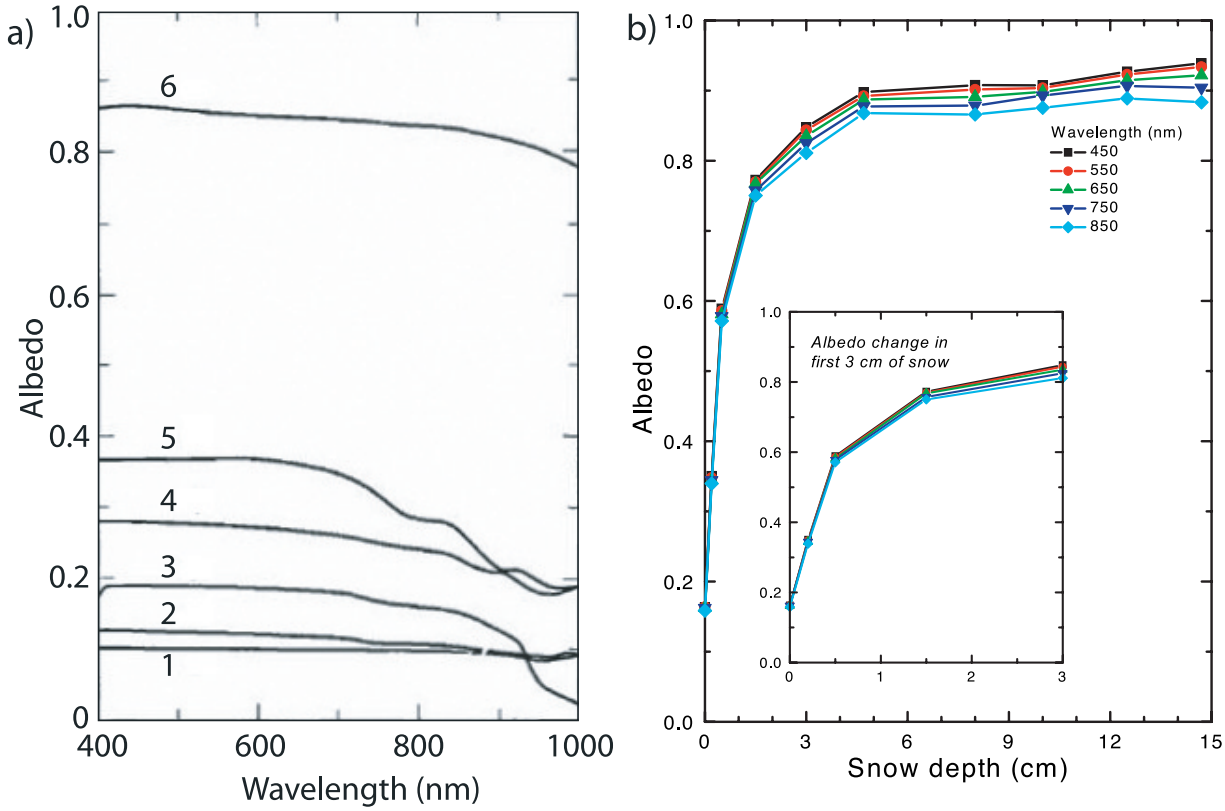

Figure 11. (a) Spectral albedos for new ice in a freezing lead. The curves are (1) wind-roughened water, (2) 2 mm skim of frazil, (3) 3-cm-thick nilas, (4) 5-cm-thick gray ice, (5) 20-cm-thick ice with no snow, and (6) 20 cm of young ice covered by 4 cm of snow. (b) Evolution of spectral albedo with increasing snow depth (provided by D. Perovich.)

with a thin layer of snow shortly (hours to days) after opening.

[29] Indeed, we have observed this rapid evolution of reflectivity in a ~25 day record of an aging lead between 29 February and 21 March 2004. Four of the 16 ICESat reflectivity/elevation profiles are shown in Figures 12c–12f. This lead, located just north of Ellesmere Island, is at a latitude that allows for repeated (near daily on occasions) ICESat observations because of the convergence of the orbits near the pole. We note that the profiles of the surrounding ice are not identical, though some features are similar, because the altimeter ground track crosses the lead at slightly different angles on each orbit. Figure 12 shows the reflectivity of the lead samples increases from 0.25 to 0.5 within ~2 days (~30 orbits, 14 orbits/day) while the reflectivity of adjacent ice cover remains nearly constant. On the fifth day, the reflectivity of the lead is almost indistinguishable from that of the adjacent thick ice. This suggests a basis for identifying samples of thin ice and open water in ICESat data, i.e., low reflectivity at dips in elevation. Even though *Kwok et al.* [2004] demonstrated the potential of using sequential RADARSAT imagery to locate new openings on the ice cover, this exclusive use of ICESat data would allow for a simpler procedure for identifying thin areas and less dependence on the time-consuming process of locating openings in sequential SAR imagery.

[30] It is also interesting to note that the average freeboards on the left and the right of the ice, relative to the average ICESat elevation in the lead, are relatively consistent over the period. The left side has a slightly lower freeboard than the right side. Some variability is expected because the ICESat ground tracks do not sample the same ice features during this period. With the freeboard at ~60 cm and an expected snow depth of ~30 cm [*Warren et al.*, 1999], a rough estimate of the thickness of 3 m is not unreasonable for this part of the ice cover.

6.2. Open Water/Near-Specular Returns

[31] Open water and very smooth surfaces have distinctive signatures in ICESat profiles because of saturation issues discussed earlier. The two examples in Figure 13

Figure 12. Evolution of reflectivity of a new lead over a period of 20 days. (a, b) RADARSAT images before (28 February) and after (3 March) the opening of the lead. ICESat elevation/reflectivity profiles over the same lead on (c) 29 February, (d) 1 March, (e) 4 March, and (f) 21 March. (g) Time-dependent reflectivity of the opening. (h) Average freeboard of the ice cover on the left and right sides of the lead. Freeboard is referenced to the elevation of the lead samples. The lead is sampled 16 times by ICESat over this period. There are approximately 14 orbits/day (RADARSAT imagery ©CSA 2004).

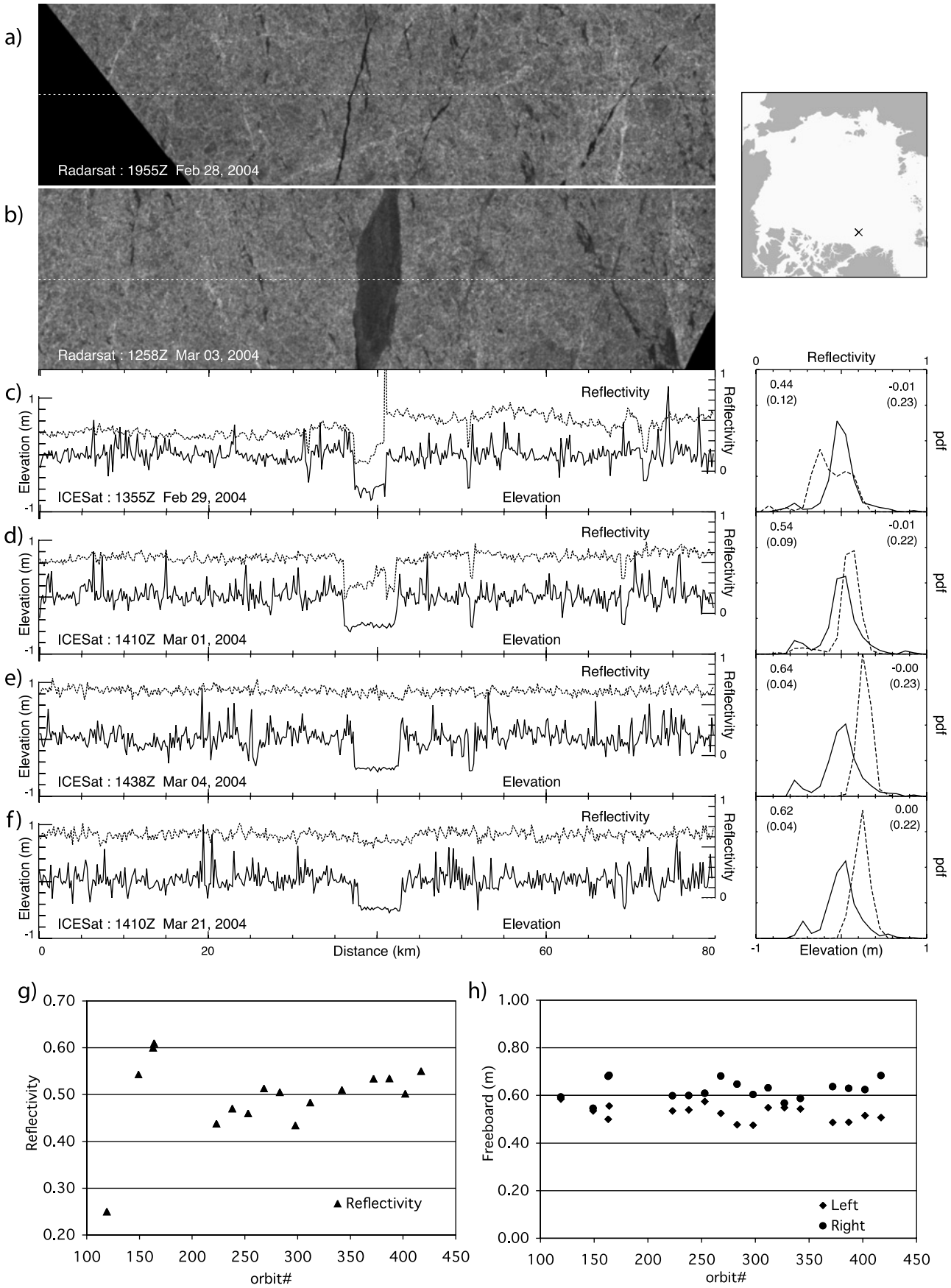
a)
Radarsat : 1955Z Feb 28, 2004
b)
Radarsat : 1258Z Mar 03, 2004
c)
ICESat : 1355Z Feb 29, 2004
d)
ICESat : 1410Z Mar 01, 2004
e)
ICESat : 1438Z Mar 04, 2004
f)
ICESat : 1410Z Mar 21, 2004
Reflectivity
Elevation
Elevation (m)
Distance (km)
0.44 (0.12)
-0.01 (0.23)
0.54 (0.09)
-0.01 (0.22)
0.64 (0.04)
-0.00 (0.23)
0.62 (0.04)
0.00 (0.22)
pdf
Elevation (m)
g)
Reflectivity
orbit#
h)
Freeboard (m)
Left
Right
orbit#

Figure 12

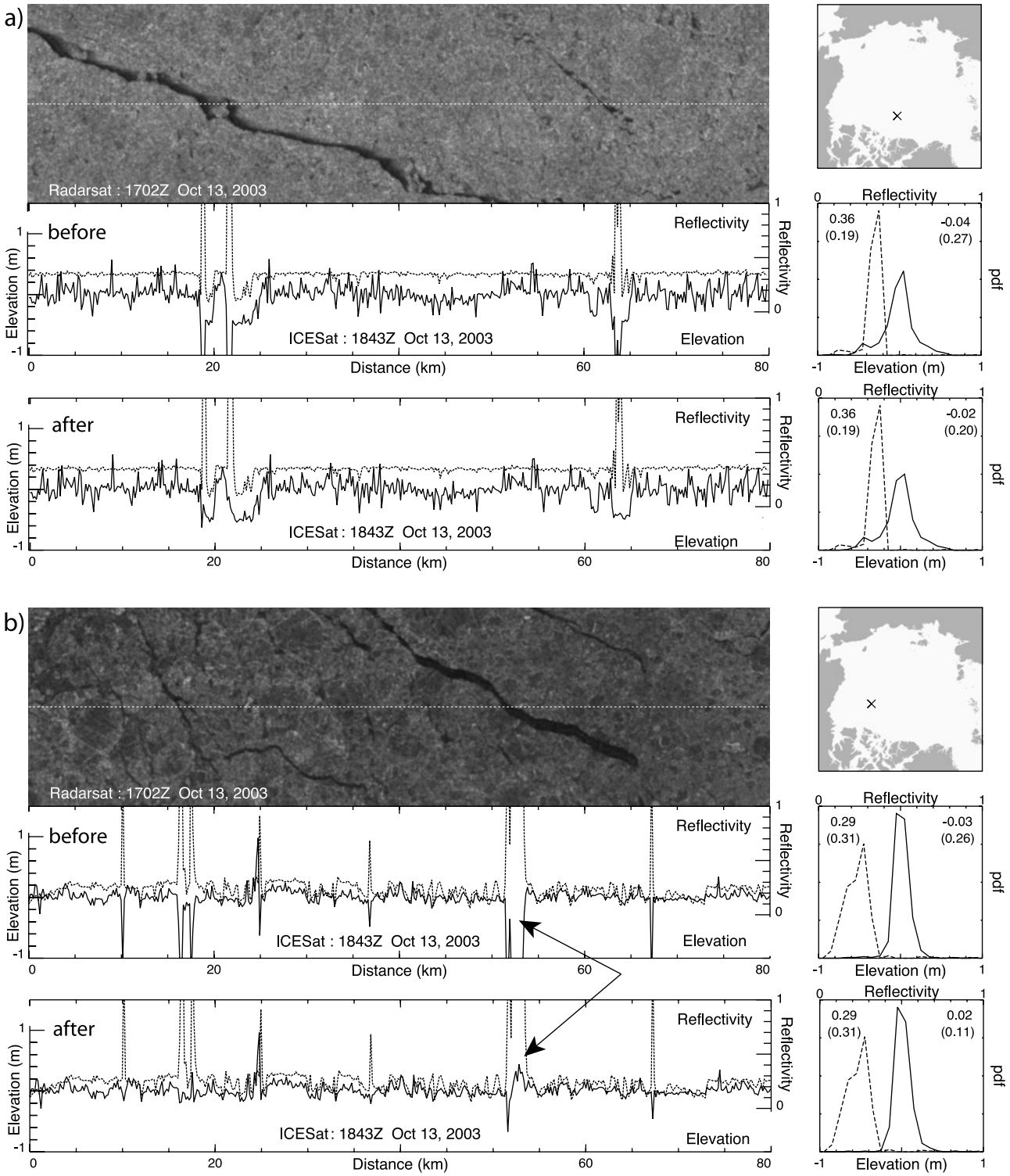

Figure 13. (a, b) Two examples of near-coincident RADARSAT and ICESat data takes over open water. The waveforms from open water are sometimes saturated due to their near-specular returns. The reflectivity/elevation are incorrectly retrieved in these cases. For received echo power >9 fJ, an a posteriori adjustment to the elevation (discussed in the text) is applied to compensate for the retrieval biases. The elevation profiles before and after the echo power-dependent corrections are shown here. Elements of the figure are the same as in Figure 10.

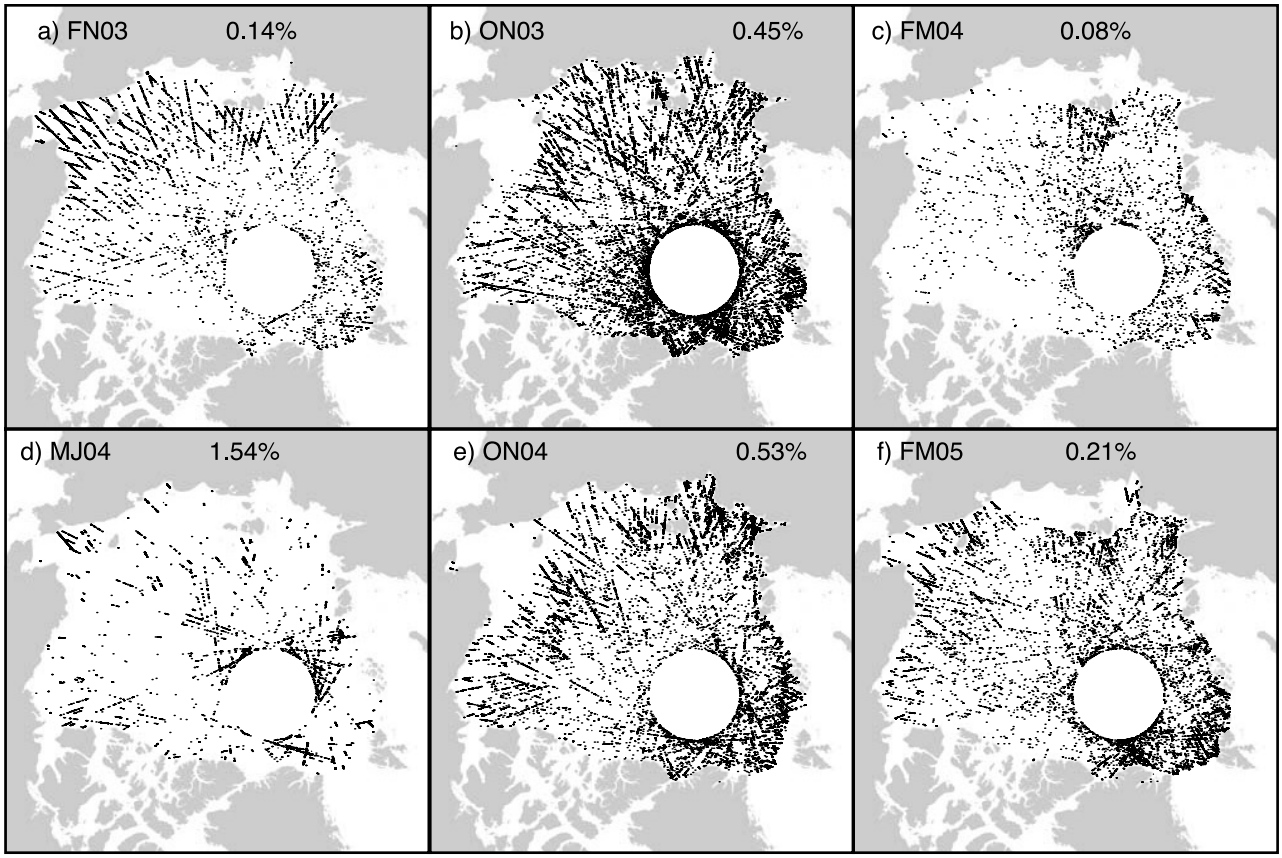

Figure 14. Spatial distribution and fraction of elevation samples with reflectivity >1. (a) FM03. (b) ON03. (c) FM04. (d) MJ04. (e) ON04. (f) FM05.

show ICESat samples from leads that are most likely due to near-specular surface returns with unphysical reflectivity (>1) coupled with unrealistic negative spikes in elevation (>1 m). These erroneous estimates are caused by applying routine elevation and reflectivity retrieval procedures to waveforms distorted by saturation. On the basis of our survey of RADARSAT/ICESat data, these types of returns are almost always found in newly opened leads. Most likely, these near-specular returns are associated within open water, grease ice, or ice types with very smooth surfaces in leads, and these surface must be smooth and oriented at almost zero incidence relative to the laser source. Examination of the seasonal distribution of these data samples ($R > 1$) show that the occurrence of these types of returns to be higher in the fall and late spring than winter (Figure 14). Fractional coverage is between 0.45–0.53% in the fall and 0.08–0.21% in the winter. The higher fraction of these types of returns in late fall and spring lends credence to our observation that most of these returns are from open leads.

[32] For received echo power >9 fJ, an a posteriori adjustment to the elevation (discussed earlier) is applied to compensate for retrieval biases (i.e., the negative spikes) due to saturation distortions. It is important to point out that saturation affects all returns (>9 fJ) and not just near-specular returns discussed here even though the issue is more acute for near-specular ones. The effectiveness of these corrections can be seen in the examples shown here. After the corrections are applied to the altimeter profiles in Figure 13a, the retrieved elevations are now more consistent with the elevation of neighboring lead samples. However, the elevation samples in one of the leads in Figure 13b (identified by a black arrow) seem to be overcorrected relative to the local mean elevation. In this case, the echo power is much greater than 50 fJ, (compared to the mean of 10 fJ for the FM04 period) and the correction is over 1.5 m. This level of saturation is probably beyond the range of valid adjustments for the equations presented in section 2. In any case, caution is prompted when using samples with reflectivity greater than unity.

6.3. Flat Ice

[33] By flat ice, we refer to sea ice that have not been subjected to any significant mechanical deformation such as ridging and/or fracture and is relatively uniform in thickness. Large areas of these types of ice can be found typically in sheltered first-year ice formed in the passages and straits within the Canadian Archipelago, and the first-year ice just north of Siberia in the southern E. Siberian and Laptev Seas. Two examples of relatively flat ice, one just west of Bathurst Island and the other just south of the Anjou Islands are shown in Figure 15. The standard deviation of the flat ice in Figure 15a (within the segment between the arrowheads and bounded by higher backscatter multiyear ice in the SAR imagery) is ~2 cm and the less "flat" segment in Figure 15b is 5 cm. These results can be comparable to the variability of the extremely flat ice over Lake Vostok, Antarctica of 2 cm; and consistent with the 1.5 cm range

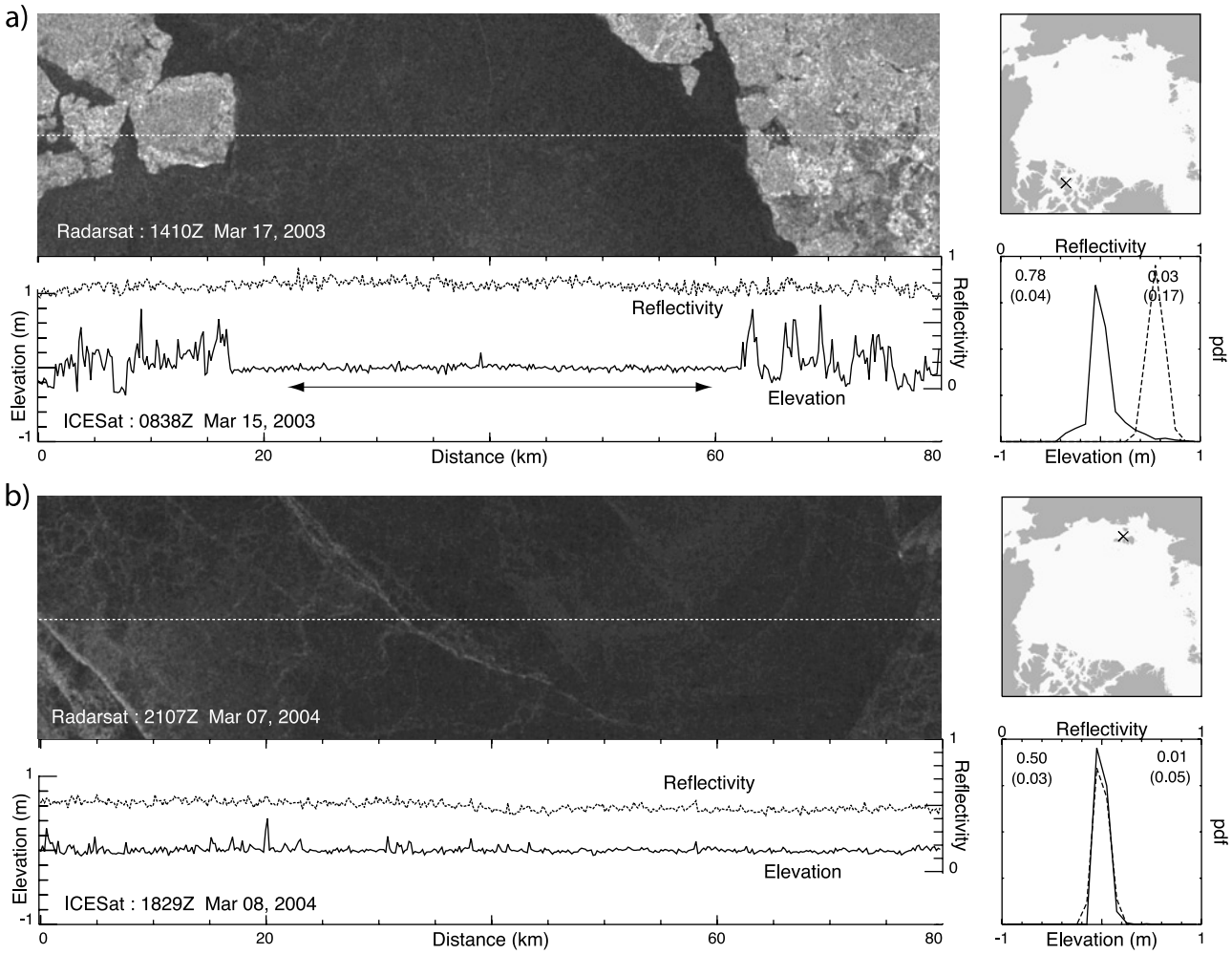

Figure 15. (a, b) Two examples of near-coincident RADARSAT and ICESat data takes over relatively flat sea ice. Elements of the figure are the same as in Figure 10.

precision in a preflight test. This provides a measure of the consistency in the noise level from the elevation retrieval process.

[34] To obtain a larger-scale assessment of this noise level, we examine the population with the smallest roughness measure in the roughness distributions over the FM03 period. Our surface roughness measure is the standard deviation of the detrended ICESat elevations over a 10 km (~60 samples) window. Again, the lower limit in the observed roughness is in the range ~1.5–2 cm: an indication of the precision in retrieval over smooth surfaces.

6.4. Ridges

[35] As shown in Figures 16a and 16b, ridges or ridge zones can be seen as distinct peaks/spikes in ICESat profiles. The two examples shown here are both from coastal Alaska and Siberia where large shear and pressure ridges are usually found. Because of the GLAS footprint size compared to the width of ridges (meters), these spikes (>0.5 m) in elevation are probably due to returns from multiple ridges rather than from an individual ridge. Whether these are due to single or multiple ridges, they appear as long linear features in SAR imagery with higher radar backscatter than that of the surrounding ice. In the past, it has always been thought that these features were associated with ridges [*Vesecky et al.*, 1990], but we believe that this is the first observed correlation between spikes in surface elevation and SAR backscatter. This is complementary to the linear relation between the draft of ridges (from sonar measurements) and radar backscatter observed by *Melling* [1998]. The higher radar backscatter from ridges can be attributed to the following factors: (1) the lower salinity and density, and higher porosity (due to weathering) enhancing volume scattering and (2) the orientation of a certain fraction of surface facets of the piled up ice blocks toward the radar and reducing the local incidence angles. Consequently the backscatter energy of ridges is typically higher than the surrounding level ice.

[36] Ridges, once they are formed by convergence or shear, influence the local momentum exchange between the atmosphere and sea ice. The amount of form drag is proportional to the mean ridge height and ridge density [*Burns*, 1990]; drag is also dependent on ridge orientations relative to the prevailing wind. In both examples shown here, the relative orientations of the ridges are not random but are aligned with the coast. These spatially varying drag coefficients and orientations affect the small- and large-scale responses of the ice cover to near surface winds that

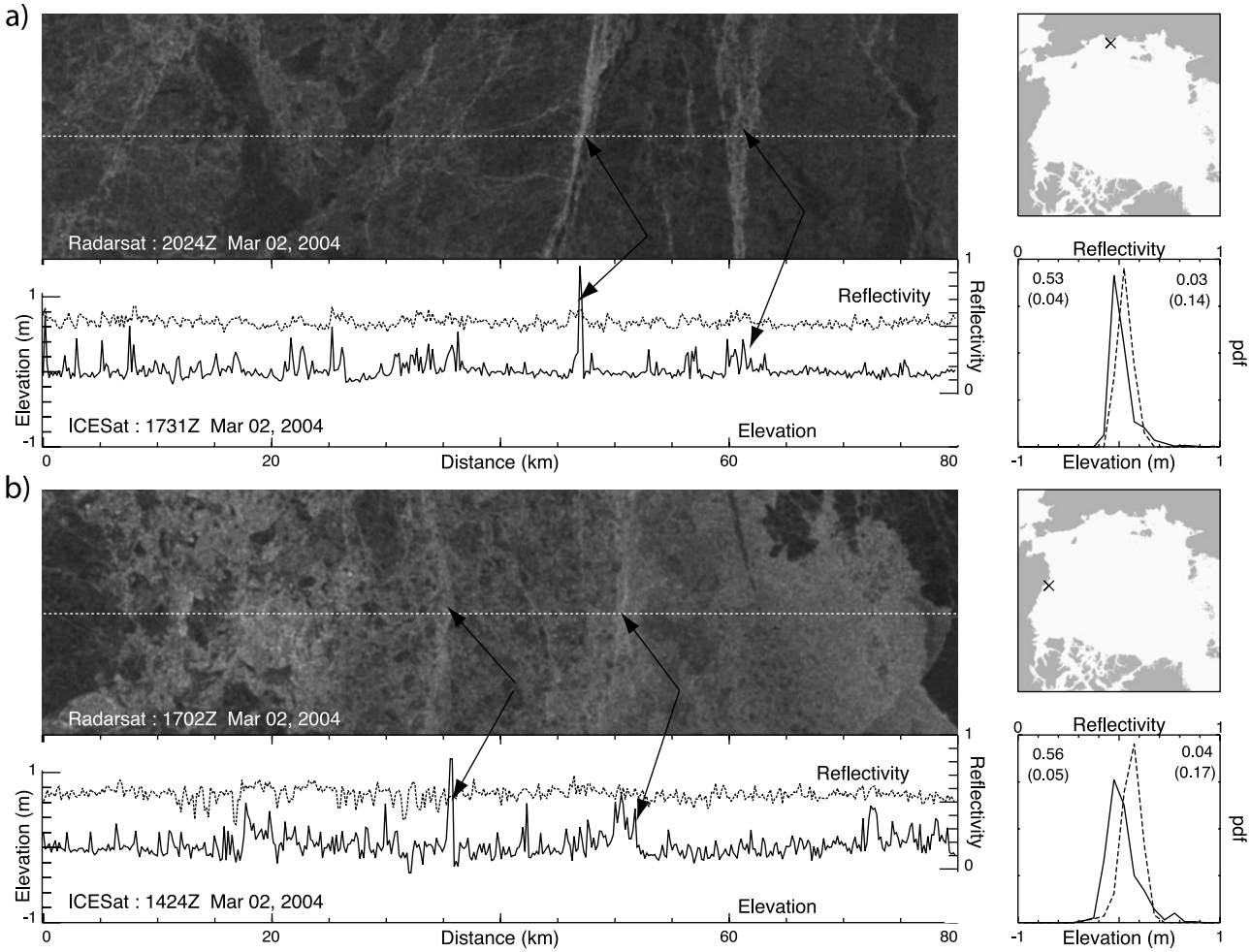

Figure 16. (a, b) Two examples of near-coincident RADARSAT and ICESat data takes over ridged ice. Elements of the figure are the same as in Figure 10.

result in gradients in small-scale ice motion and stress distributions within the ice cover. The use of these coincident data sets to improve the understanding of the variability of surface drag, although outside the scope of the present analysis, is worthy of closer examination.

6.5. ICESat Waveforms

[37] Figure 17 contrasts the ICESat waveforms from five surface types: first-year (FY) ice, multiyear (MY) ice, thin ice (grey) in new openings, open water or near specular surface, and ridges or ridge zones. The waveforms from FY and MY ice (Figures 17a and 17b), unless there is large-scale roughness due to surface relief (e.g., hummocks, rafted ice, ridges) within a footprint, look similar as their surface returns are mostly dominated by the properties of the snow cover. This can be seen in the characteristic broadening of the return pulse associated with that of ridges (Figure 17e). Thus a range of broadening due to surface relief can be expected. Even though the reflectivity is fairly uniform over the ice cover (except for the new opening in Figures 17c and 17d and other examples shown in this paper), waveform characteristics can perhaps be used to estimate the surface height distribution within an illuminated spot of the laser altimeter. New ice (Figure 17c), as discussed above, has a waveform shape that is not far from that of smooth FY and MY ice (Figures 17a and 17b); only that the reflectivity is lower.

[38] The saturation issue is clearly illustrated in Figure 17d. This is likely associated with open water or a near specular surface as discussed earlier. The top of the waveform is truncated leading to a characteristic overestimation in reflectivity and an underestimation of the elevation, artifacts of the waveform fitting process described earlier. Saturation of these surface samples in new openings is unfortunate because they could have served as unambiguous sea level references for retrieval of sea ice freeboard.

7. Conclusions

[39] The present examination of the utility of ICESat data for studies of the Arctic Ocean is by no means exhaustive. It represents a more detailed assessment, compared to the first look offered by *Kwok et al.* [2004] of the quality and the potential of the data set; these first steps are important for understanding the capabilities and limitations of the instrument for making observations of the sea ice cover and the polar oceans. In this section, we summarize the salient points.

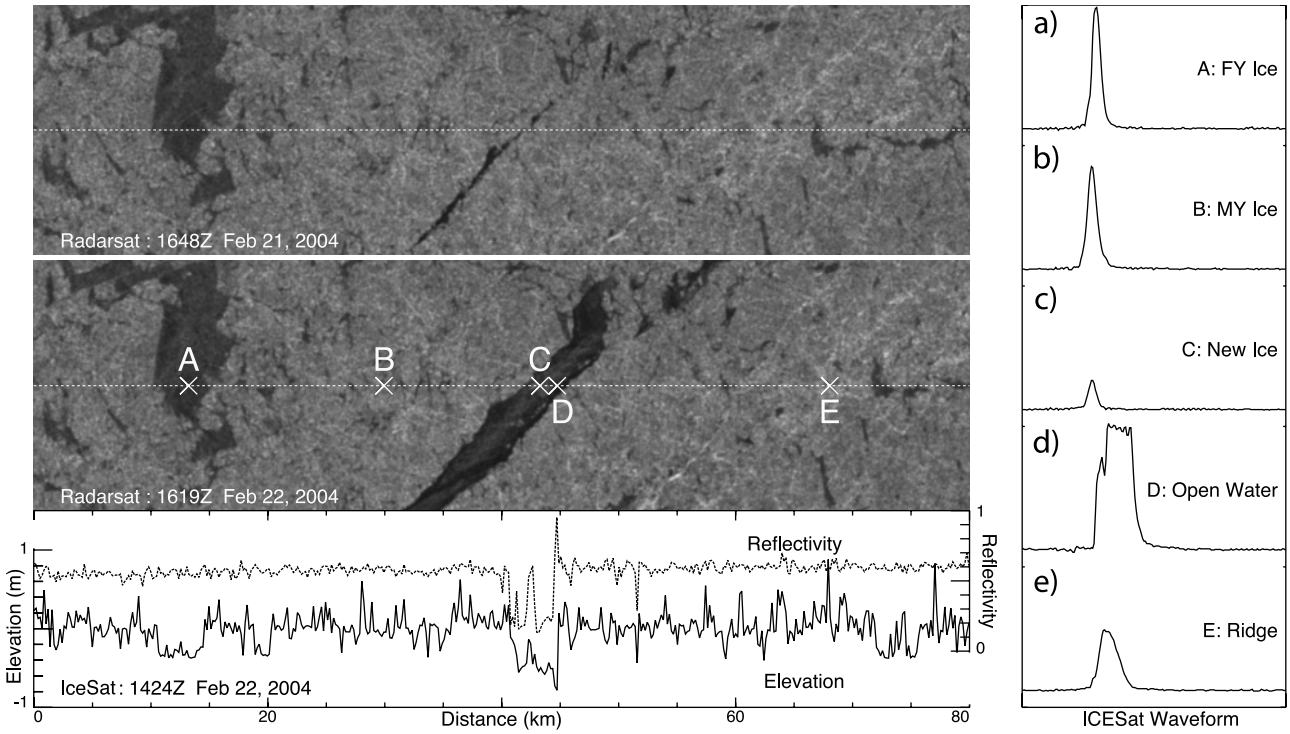

Figure 17. ICESat waveforms over different sea ice surfaces. (a) First-year ice. (b) Multiyear ice. (c) New ice. (d) Open water. (e) Ridges. The waveform plots do not share the same vertical scale.

[40] An issue that affects the ICESat elevations is the saturation of the GLAS instrument. The distortion of the waveform depends on echo energy; all returns with energy >9 fJ are affected by some level of saturation. On the basis of ground testing, moderate levels of saturation and their effects on elevation retrieval are predictable and can be corrected. Examples here show that these corrections seem effective. However, the level of saturation of waveforms from high reflectivity and near-specular returns are beyond the range of valid adjustments. In these cases, caution should be exercised in using these elevation samples.

[41] On a broad scale, residual signals of the geoid, the atmosphere, tides, and dynamic topography in the ICESat profiles are discussed. Response of the sea ice cover to the inverted barometer effect is near ideal. It is evident that the IB correction significantly decreases the variance of the ICESat fields and is an important step in using the data. By far, the residuals are dominated by geoidal height. This can be seen in the consistency of the spatial patterns of the residual fields (Figure 5) from all six surveys. Features in the residual fields correspond to bathymetric relief with high surface slopes. This suggests that these residuals could be, in turn, used to improve the representation of smaller-scale features in the Arctic geoid. A number of investigators are moving in this direction. The variability of the observed elevation due to dynamic topography remains a question. On the basis of the magnitude of these residuals, it is clear that frequent sea level references are required for accurate determination of freeboard.

[42] Seasonal and interannual differences in ICESat elevations are consistent with expectations, i.e., winter–fall > 0. Since basal ice growth is slower over thick multiyear ice, the larger contribution of snow depth to sea ice freeboard suggests that it may be possible to obtain some level of estimate of the snow depth over MY ice because ice growth over MY ice can be roughly modeled. A denser temporal sampling of the ice cover would provide a more usable trend in freeboard for surface heat balance calculations and the development of a better snow climatology.

[43] At the small scale, RADARSAT imagery provides a spatial context, along with the vertical dimension of the altimeter profiles, for better interpretation of the small-scale characteristics of the ICESat elevations. In one examination, the steep increase in reflectivity in a new opening is consistent with the prompt coverage by a snow layer. In situ observations support that only 1–2 cm of snow cover is required to nearly mask the reflectivity of the underlying ice; this snow-covered thin ice is indistinguishable from the adjacent snow cover. Thin ice is thus likely when coincident dips in reflectivity and elevations are encountered in ICESat samples. This suggests an algorithmic basis for identifying samples of thin ice and open water in ICESat data, i.e., low-reflectivity samples are associated with samples of thin ice. Even though *Kwok et al.* [2004] demonstrated the use of sequential RADARSAT imagery to locate new openings in the ice cover, this exclusive use of ICESat data would allow for a simpler procedure for identifying thin ice areas and less dependence on the time-consuming process of locating openings in sequential SAR imagery.

[44] In the past it has always been thought that high backscatter linear features were associated with ridges, but we believe that this is the first observed correlation between spikes in surface elevation in ICESat profiles and SAR backscatter. This is complementary to the linear relation between the draft of ridges and radar backscatter observed by *Melling* [1998]. Ridge zones (or keels) modify the air/

water stress components in the momentum balance and create gradients in small-scale ice motion and stress distributions within the ice cover. Although outside the scope of the present analysis, the use of these coincident data sets to improve the understanding the variability of surface drag is worthy of closer examination.

[45] ICESat observations over the Arctic Ocean show promise in providing a variety of geophysically useful sea ice observations. It is unfortunate that the limitations of the laser lifetime have not permitted the originally intended continuous operation, but the revised measurement strategy is providing multiyear observations with surveys of 33 days each during winter, spring, and fall. Of immediate geophysical interest is the development of a robust procedure, with quantifiable uncertainties, for location of the sea surface that allows for better separation of the processes embedded in the retrieved elevation and the estimation of sea ice freeboard.

[46] **Acknowledgments.** The RADARSAT image data are provided by the Alaska Satellite Facility, Fairbanks. The Special Sensor Microwave Imager brightness temperature and ice concentration fields are provided by World Data Center A for Glaciology/National Snow and Ice Data Center, University of Colorado, Boulder. ICESat data are from the ICESat Science Team Computing Facility and NSIDC. This work was carried out at the Jet Propulsion Laboratory, California Institute of Technology under contract with NASA and at the Goddard Space Flight Center supported by the ICESat Science Project.

References

Brenner, A. C., et al. (2000), Derivation of range and range distributions from laser pulse waveform analysis for surface elevations, roughness, slope, and vegetation heights, algorithm theoretical basis document, vers. 3.0, Goddard Space Flight Cent., Greenbelt, Md.

Burns, B. A. (1990), SAR image statistics related to atmospheric drag over sea ice, *IEEE Trans. Geosci. Remote Sens.*, *28*(2), 158–165.

Chelton, D. B., J. C. Ries, B. J. Haines, L. Fu, and P. S. Callahan (2001), Satellite altimetry, in *Satellite Altimetry and Earth Sciences*, *Int. Geophys. Ser.*, vol. 19, pp. 1–131, Elsevier, New York.

Cudlip, W., D. R. Mantripp, C. L. Wrench, H. D. Griffiths, D. V. Sheehan, M. Lester, R. P. Leigh, and T. R. Robinson (1994), Corrections for altimeter low-level processing at the Earth Observation Data Centre, *Int. J. Remote Sens.*, *15*, 889–914.

Eanes, R. J. (1994), Diurnal and semidiurnal tides from TOPEX/Poseidon altimetry, *Eos Trans. AGU*, *75*(16), Spring Meet. Suppl., abstract G31A-6.

Forsberg, R., and H. Skourup (2005), Arctic Ocean gravity, geoid and sea-ice freeboard heights from ICESat and GRACE, *Geophys. Res. Lett.*, *32*, L21502, doi:10.1029/2005GL023711.

Kalnay, E., et al. (1996), The NCEP/NCAR 40-year reanalysis project, *Bull. Am. Meteorol. Soc.*, *77*, 437–471.

Kenyon, S., and R. Forsberg (2001), Arctic Gravity Project: A status, in *Gravity, Geoid and Geodynamics 2000*, *Int. Assoc. Geod. Symp.*, vol. 123, edited by M. G. Sideris, pp. 391–395, Springer, New York.

Kowalik, Z., and A. Y. Proshutinsky (1994), The Arctic Ocean tides, in *The Polar Oceans and Their Role in Shaping the Global Environment*, *Geophys. Monogr. Ser.*, vol. 85, edited by O. M. Johannessen et al., pp. 137–158, AGU, Washington, D. C.

Kwok, R. (2004), Annual cycles of multiyear sea ice coverage of the Arctic Ocean: 1999–2003, *J. Geophys. Res.*, *109*, C11004, doi:10.1029/2003JC002238.

Kwok, R., H. J. Zwally, and D. Yi (2004), ICESat observations of Arctic sea ice: A first look, *Geophys. Res. Lett.*, *31*, L16401, doi:10.1029/2004GL020309.

Le Provost, C., F. Lyard, J. M. Molines, M. L. Genco, and F. Rabilloud (1998), A hydrodynamic ocean tide model improved by assimilating a satellite altimeter-derived data set, *J. Geophys. Res.*, *103*, 5513–5529.

Marshall, J., A. Adcroft, C. Hill, L. Perelman, and C. Heisey (1997), A finite-volume, incompressible Navier-Stokes model for studies of the ocean on parallel computers, *J. Geophys. Res.*, *102*, 5753–5766.

Melling, H. (1998), Detection of features in first-year pack ice by synthetic aperture radar, *Int. J. Remote Sens.*, *19*, 1223–1240.

Menemenlis, D., et al. (2005), NASA supercomputer improves prospects for ocean climate research, *Eos Trans. AGU*, *86*(9), 89.

Peacock, N. R., and S. W. Laxon (2004), Sea surface height determination in the Arctic Ocean from ERS altimetry, *J. Geophys. Res.*, *109*, C07001, doi:10.1029/2001JC001026.

Pihos, G. (1994), Determining the response of sea level to atmospheric pressure forcing using TOPEX/Poseidon data, *J. Geophys. Res.*, *99*, 24,633–24,642.

Ray, R. D. (1999), A global ocean tide model from Topex/Poseidon altimetry: GOT99.2, *NASA Tech. Memo., 209478*, 58 pp.

Shum, C. K., et al. (1997), Accuracy assessment of recent ocean tide models, *J. Geophys. Res.*, *102*, 25,173–25,194.

Smith, S. R., D. M. Legler, and K. V. Verzone (2001), Quantifying uncertainties in NCEP reanalyses using high-quality research vessel observations, *J. Clim.*, *14*(20), 4062–4072.

Sun, X., J. B. Abshire, and D. Yi (2003), Geoscience Laser Altimeter System: Characteristics and performance of the altimeter receiver, *EOS Trans. AGU*, *84*(46), Fall Meet. Suppl., Abstract C32A-0432.

Tapley, B. D., et al. (2004), GRACE measurements of mass variability in the Earth system, *Science*, *305*(5683), 503–505.

Untersteiner, N. (1961), On the mass and heat budget of Arctic sea ice, *Arch. Meteorol. Geophys. Bioklimatol., Ser. A*, *12*, 151–182.

Vesecky, J. F., M. P. Smith, and R. Samadani (1990), Extraction of lead and ridge characteristics from SAR images of sea ice, *IEEE Trans. Geosci. Remote Sens.*, *28*(4), 740–744.

Wagner, C. (1979), The geoid spectrum from altimetry, *J. Geophys. Res.*, *84*, 3861–3871.

Warren, S. G., I. G. Rigor, N. Untersteiner, V. F. Radionov, N. N. Bryazgin, Y. I. Aleksandrov, and R. Colony (1999), Snow depth on Arctic sea ice, *J. Clim.*, *12*(6), 1814–1829.

Wunsch, C., and D. Stammer (1997), Atmospheric loading and the oceanic "inverted barometer" effect, *Rev. Geophys.*, *35*, 79–107.

Yi, D., X. Sun, and H. J. Zwally (2003), A study of the GLAS echo waveform using ground test data, *Geophys. Res. Abstr.*, *5*, 13690.

Zwally, H. J., et al. (2002), ICESat's laser measurements of polar ice, atmosphere, ocean, and land, *J. Geodyn.*, *24*, 405–445.

G. F. Cunningham and R. Kwok, Jet Propulsion Laboratory, California Institute of Technology, 4800 Oak Grove Drive, Pasadena, CA 91109, USA. (ron.kwok@jpl.nasa.gov)

D. Yi, SGT, Inc., Goddard Space Flight Center, Greenbelt, MD 20771, USA.

H. J. Zwally, Cryospheric Sciences Branch, Code 614.1, Goddard Space Flight Center, Greenbelt, MD 20771, USA.